



HAL
open science

Discontinuous Shear Thickening (DST) transition with spherical iron particles coated by adsorbed brush polymer

Georges Bossis, Yan Grasselli, Olga Volkova

► **To cite this version:**

Georges Bossis, Yan Grasselli, Olga Volkova. Discontinuous Shear Thickening (DST) transition with spherical iron particles coated by adsorbed brush polymer. *Physics of Fluids*, 2022, 34 (11), pp.113317. 10.1063/5.0120502 . hal-03864518v2

HAL Id: hal-03864518

<https://hal.science/hal-03864518v2>

Submitted on 6 Mar 2023

HAL is a multi-disciplinary open access archive for the deposit and dissemination of scientific research documents, whether they are published or not. The documents may come from teaching and research institutions in France or abroad, or from public or private research centers.

L'archive ouverte pluridisciplinaire **HAL**, est destinée au dépôt et à la diffusion de documents scientifiques de niveau recherche, publiés ou non, émanant des établissements d'enseignement et de recherche français ou étrangers, des laboratoires publics ou privés.

Discontinuous Shear Thickening (DST) transition with spherical iron particles coated by adsorbed brush polymer

Georges Bossis^{1,a)}, Yan Grasselli^{1,2,b)}, Olga Volkova^{1,c)}

¹ Institute of Physics of Nice, Université University Côte d'Azur, Parc Valrose, CNRS UMR 7010, 06108, Nice, France

² Université University Côte d'Azur SKEMA Business School, 60 rue Dostoievski, CS30085, Sophia Antipolis, 06902, Valbonne, France

a) Author to whom correspondence should be addressed : georges.bossis@unice.fr

b) yan.grasselli@skema.edu

c) olga.volkova@unice.fr

ABSTRACT

We explore the rheology of very concentrated ($0.55 < \Phi < 0.67$) suspensions of carbonyl iron (CI) particles coated by a small polymer. A strong discontinuous shear thickening (DST) is observed in a large range of volume fraction presenting some specific behaviours in comparison to other systems. In particular, the DST transition can appear suddenly without being preceded by shear thickening. The presence of a frictional network of particles is confirmed by a simultaneous measurement of the electric resistance of the suspension and of the rheological curve. Using the Wyart-Cates(W-C) model we show that with increasing the volume fraction, the fraction of frictional contacts increases more quickly with the stress, contrary to the prediction of numerical simulations. The same behaviour is observed in the presence of a magnetic field with a strong increase of the viscosity before the DST transition. We interpret this behaviour by the interpenetration of the polymer layer under the effect of the shear stress -and of the magnetic stress- followed by the expulsion of the polymer out of the surfaces between two particles in contact. We point out that above the DST transition, we do not observe a jamming in the range of volume fraction whereas it is predicted by the W-C model. The frictional contacts are created by a shear stress and not by a static stress, so in the absence of shear flow, the polymer can adsorb again on the surface and lubricate the frictional contacts. We thus predict an asymptotic non-zero shear rate reproducing the experimental behaviour.

I. INTRODUCTION

The rheology of suspensions of particles is of ubiquitous importance in many industrial processes where it is needed to find a compromise between a large volume fraction of solid particles to obtain a strong material and to minimize subsequent drying keeping a low viscosity

39 in the moulding process. Generally the viscosity of these suspensions first decreases with the
40 shear rate (shear thinning) and then increases (shear thickening) more and more abruptly as the
41 volume fraction of particles increases (for a review of pioneering works see Barnes¹). If only
42 hydrodynamic interactions between particles are present the shear rate gives a time scale but,
43 in absence of inertia, the viscosity would not depend on it. It is only through the presence of
44 other forces -entropic or deriving from a potential- that a dependence on the shear rate can
45 appear. For non-Brownian suspensions adhesive Van Der Waals forces and gravity play an
46 important role on the formation of a network of aggregated particles which can give rise to a
47 yield stress. Increasing the shear rate will contribute to break these aggregates and to decrease
48 the viscosity of the suspension. On the other hand, repulsive forces either electrostatic like those
49 due to ionic layers or entropic like those coming from an adsorbed or grafted layer of polymers
50 can prevent the aggregation. In the latter, the yield stress is decreased, and the viscosity is
51 reduced for a given volume fraction. Generally, the decrease of the viscosity is due to
52 deflocculating whereas the shear thickening is, on the contrary, due to the formation of transient
53 aggregates. The qualitative explanation being that the suspending fluid imprisoned inside the
54 aggregates behave as the solid particles and then increases the apparent volume fraction of the
55 particles and thus the viscosity. Actually, a model based on the dynamics of
56 aggregation/disaggregation can qualitatively represent the different rheological behaviour
57 observed in concentrated suspensions². In the extreme case of highly concentrated suspensions
58 the shear thickening transition can manifest by a sudden jump of stress at a given shear rate in
59 an imposed ramp of shear rate or in a sudden decrease of shear rate in a controlled stress
60 experiment. This sudden phenomenon is called discontinuous shear thickening (DST). To our
61 knowledge H. Freundlich³ was the first to present an experiment clearly showing a DST
62 transition on a paste made of quartz particles in water. More recently Hoffman⁴ conducted a
63 systematic study of the rheology of suspensions of monodisperse PVC spheres with a diameter
64 in the range 0.4-1.3 μm and volume fraction larger than 50%. The use of diffraction of white
65 light during the experiment clearly demonstrated that the transition was associated with the
66 rupture of a layered structure made of particles hexagonally packed and sliding over each other.
67 This behaviour was recovered on monodisperse suspensions of smaller particles: $d=200\text{nm}$ ⁵.
68 On the other hand this abrupt shear thickening was also observed in moderately polydisperse
69 suspensions of latex particles by Laun *et al.*⁶ and it was demonstrated, by neutron scattering in
70^{7,8} that it happens in the absence of a layered pattern preceding the transition. Using dichroism
71 measurements, d'Haene *et al.*⁹ have observed on suspensions of PMMA sterically stabilized,
72 that above the critical stress, the relaxation of the structure was much longer and deduced the
73 presence of large clusters spanning the cell. Furthermore polydisperse suspensions particles of
74 irregular shape like corn-starch¹⁰, acicular calcium carbonate¹¹ or gypsum¹² which cannot be
75 supposed to flow in regular planes also show this jump of viscosity. The DST transition can
76 happen as well for particles sterically stabilized in non-polar solvents like PMMA in aliphatic
77 hydrocarbon¹³, in di-octyl phthalate¹⁴ or stabilized by electrostatic layers in polar solvent³,
78 for quartz in water^{15,16} for silica in water;^{8,17} for silica in tetrahydrofuran;¹⁸ for polystyrene in
79 water. The onset of the transition is ruled by the competition between the shear forces and the
80 repulsive forces which prevent the surfaces to come in contact and to experiment friction forces.
81 By varying the pH in suspensions of silica or alumina at a constant salt concentration, Franks
82 *et al.*¹⁹ have shown that the increase of the magnitude of the repulsive force was increasing the
83 critical shear stress of the DST transition. The sudden contact between particles is believed to
84 provoke the formation of a network of particles acting like a solid skeleton able to support the
85 stress through elastoplastic contacts. This network is a transient one and its rupture and
86 reformation with the strain manifests through huge fluctuations of the stress if the shear rate is
87 imposed¹⁶ or of the shear rate if the stress is imposed²⁰ as also pointed by other authors^{8,9,18}.
88 The presence of frictional forces was confirmed experimentally through the presence of a

89 positive normal stress proportional to the shear stress^{10,20–23} which expresses the force exerted
 90 on the upper plate of the rheometer by quasi solids aggregates trying to rotate in a confined
 91 space. Also shear reversal experiments demonstrated that even in the continuous shear
 92 thickening domain, the elastic forces were dominant upon hydrodynamic ones²⁴. In the usual
 93 rheometric cells, there is a free surface and the particle pressure generated by the shear stress
 94 above the transition will push them outside the fluid phase; nevertheless there are maintained
 95 inside the fluid as long as the capillary pressure is larger than the particle pressure^{23,25}.
 96 Besides the experiments, numerical simulation of the trajectories of an assembly of particles is
 97 a precious tool to correlate the macroscopic observations of the rheological behaviour to the
 98 spatial reorganisation of the particles under shear. Stokesian Dynamics allows to properly
 99 consider hydrodynamic forces in concentrated suspensions and in particular the lubrication
 100 forces which play a crucial role to prevent the contacts between the surfaces of the particles. A
 101 simulation including lubrication forces and frictional ones was realized by Seto *et al.*²⁶ and Mari
 102 *et al.*²⁷ on concentrated suspensions. In their model the cut-off of the lubrication forces was
 103 taken at $10^{-3} a$ (a is the radius of the particles) and at this distance, the contact forces were
 104 introduced through normal, k_n , and tangential k_t spring stiffness with the Coulomb criteria for
 105 the tangential force: $F_t \leq \mu F_n$ where μ is the friction coefficient. It is also worthwhile to note that
 106 the presence of periodic boundary conditions prevents the dilatancy of the suspension and the
 107 simulation made at an imposed shear rate, actually shows a DST transition above a given
 108 volume fraction. The stress corresponding to the beginning of the shear thickening remains
 109 quite independent of the volume fraction-except close to the jamming one²⁸ - as expected if it
 110 results from a balance of repulsive to shear forces. This independence was also found
 111 experimentally in several works^{8,14,20,22,23,29–31}. The most important observation was the
 112 correlation between the change of the fraction of frictional contacts $f(\sigma)$ with the giant
 113 fluctuation of stress close to the DST transition showing that the transition was mostly not
 114 structural but related to the contact between the particles. The function $f(\sigma)$ had a sigmoid shape
 115 and was independent of the volume fraction. In imposed stress simulations Singh *et al.*²⁸ have
 116 compared their results to the predictions of a model of M. Wyart and Cates³² based on a
 117 jamming volume fraction $\Phi_j(\sigma)$ which can change from a lower bound depending on μ : Φ_j^μ to
 118 the maximum packing fraction of frictionless spheres Φ_0 according to a linear equation:
 119 $\Phi_j(\sigma) = f(\sigma) \Phi_j^\mu + (1 - f(\sigma)) \Phi_0$. The model was able to reproduce the numerical data both for the
 120 viscosity, the normal stress difference, and the particle pressure. Nevertheless, using this model
 121 with the values obtained for the dependence $\Phi_j^\mu(\mu)$ and different prefactors, Lee *et al.*³³ did
 122 not succeed to represent properly their experimental data on silica spheres with different
 123 coating, even with an overestimated value ($\mu=1$) of the friction coefficient. Another objection
 124 to this model is that it is possible to get a DST transition without frictional forces if the surface
 125 of the particles present asperities, as demonstrated by numerical simulation³⁴.
 126 In this paper, we are comparing the prediction of this model to experimental data
 127 obtained on a suspension of iron microparticles coated by a polymer brush. Polymer brushes
 128 make very efficient coating to prevent dry friction between the particles³⁵. Polymer brushes as
 129 surfactant, together with the use of mineral undeformable particles, provide a system more
 130 reliable than soft particles as shown in a recent work of Le *et al.*³⁶ proving that the interaction
 131 of the solvent with the surface of the particles modifies the interparticle force and rules the DST
 132 behaviour. In addition, the use of iron spheres provides a double interest: first we can measure
 133 its conductivity and we expect to observe a change when frictional contacts occur during the
 134 DST transition, second, we can add a supplementary stress through the application of a
 135 magnetic field. In this way we have already shown that it was possible to trigger the DST
 136 transition³⁷. Other possibilities to trigger the transition are to add vibrations which contribute
 137 to break the force chains³⁸ or to use a coating of microparticles with temperature responsive

138 polymers to modify the interparticle forces³⁹. In this work we shall rather use this possibility
 139 to deepen our understanding of the DST transition.

140 In section II we shall present the suspension used and the determination of its theoretical
 141 maximum flowing volume fraction Φ_0 . In section III we shall describe the experimental results
 142 in the absence of a magnetic field and demonstrate the existence of a percolated network of
 143 frictional contacts through the measurement of the electric resistance of the sample during a
 144 ramp of shear rate. Then we shall look at the dependence of stress-shear rate curves versus the
 145 volume fraction and will see to which extent it is possible to reproduce them with the model of
 146 Wyart and Cates. We shall also propose some modifications of this model to explain the absence
 147 of jamming at high volume fraction. At last, in section IV, looking at the change of DST with
 148 the magnetic field we shall see if it is possible to get a coherent view of these experimental data,
 149 taking into account the interpenetration of the the polymer layers.

150 II. MATERIALS

151 The particles we used are made of carbonyl iron obtained from BASF (grade HQ); they have a
 152 density $\rho=7.7\text{g/cm}^3$ measured with a gas pycnometer and are currently used for making
 153 magnetorheological suspensions. Their size distribution was obtained with the help of several
 154 images taken by scanning electron microscopy (SEM). The samples were mounted on a SEM
 155 stub with carbon tape and subsequently coated with platinum (3 nm) prior to observations,
 156 performed with a JEOL JSM 6700F SEM at an accelerating voltage of 3 kV. A total of 2300
 157 particles were analysed with ImageJ. From this size distribution, the first moment is the mean
 158 radius: $M_1 = \langle a \rangle = 0.296\mu\text{m}$ and the standard deviation is $\sigma_{\text{std}} = 0.15\mu\text{m}$. A representative SEM
 159 image is shown in Fig 1(a) and the experimental size distribution in Fig. 1(b) together with its
 160 fit by a lognormal distribution for the density of probability to find a radius a_i in a class i of
 161 thickness 0.05mm:

$$162 \quad P(x) = \frac{1}{x\sigma\sqrt{2\pi}} \exp\left[-\frac{(\ln x + 0.5\sigma^2)^2}{2\sigma^2}\right] \quad (1)$$

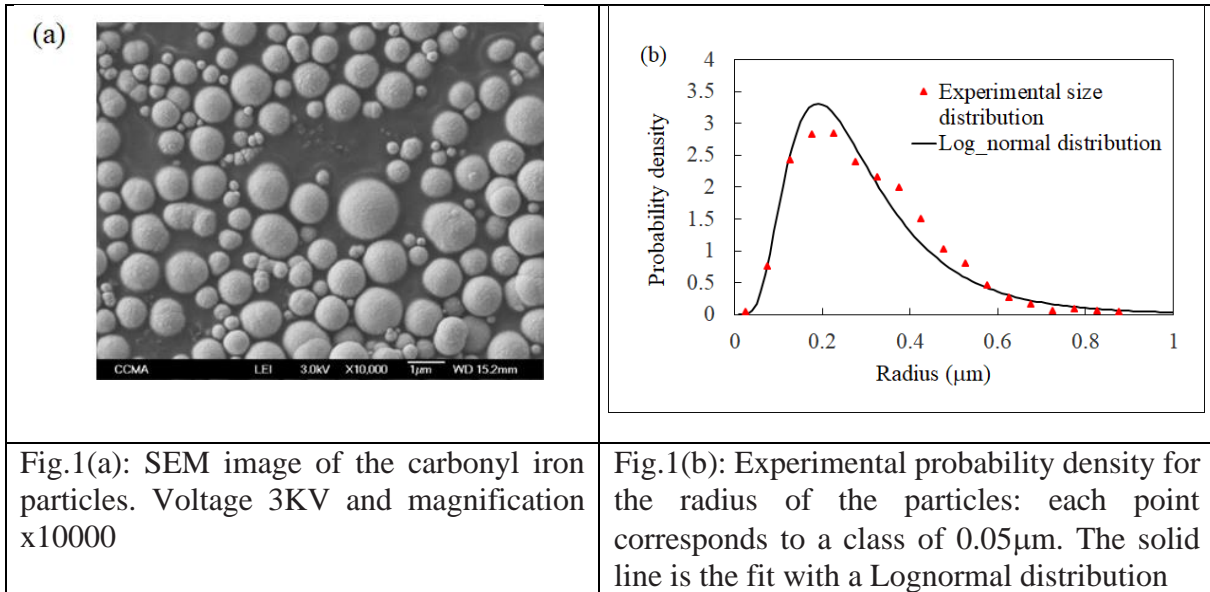
163 Here $x = a/\langle a \rangle$. The parameter of the fit is $\sigma=0.547$. The moments of the size distribution are:
 164 $M_k = \int_0^\infty a^k P(a) da$ (2)

165
 166 Using SEM pictures, we do not consider the thickness of the polymer layer which prevents the
 167 aggregation of the particles. This polymer is a superplasticizer molecule whose commercial
 168 name is Optima 100 made of a short polyethylene oxide (PEO) chain (in average 44 O-CH₂CH₂
 169 groups) and a diphosphonate head with sodium counter ions. As in a preceding work where we
 170 have used it with calcium carbonate particles we shall name it PPP44⁴³. It is the phosphonate
 171 head negatively charged which binds electrostatically with the iron surface. In all the
 172 suspensions, the mass of PPP44 used was 2mg/g of iron which is slightly larger than the
 173 concentration corresponding to the inflexion of the adsorption isotherm marking the realization
 174 of the first layer of polymer on the surface of the particles. The thickness of the layer can be
 175 approximated by the gyration radius of the polymer in a good solvent which is $d=b.P^{3/5}$ with
 176 $b=0.526\text{nm}$ the Kuhn length of the PEO group and $P=44$ the number of monomers; we obtain
 177 $d=5.1\text{nm}$. The third moment of the distribution is proportional to the volume of the solid, so
 178 taking $(a+\delta)^3$ instead of a^3 we obtain for the real volume fraction of the solid phase:

$$179 \quad \Phi_{\text{eff}} = \frac{1}{1 + \frac{M_3(1-\phi)}{M_3\delta\phi}} \quad (3)$$

180 where $M_3=0.0642$ and $M_{3\delta}=0.066$ are respectively the moments of the experimental
 181 distribution based on a^3 and $(a+\delta)^3$. The different volume fractions are calculated from the

182 density of the iron particles and of the suspending fluid and corrected with the help of Eq. (3)
 183 when they are used in the rheological models.
 184



185
 186 Last, the suspending liquid is a mixture of ethylene glycol and water (respectively 85% and
 187 15% in mass) whose composition was chosen to minimize the evaporation rate. The viscosity
 188 of the suspending fluid at 20°C was $\eta_f=11.8\text{mPa}\cdot\text{s}$. The suspension was stirred with a vortex
 189 mixer during 5mn, then placed in an ultrasound bath for 10 min, and stirred again for 5 min
 190 with the vortex mixer. Then the suspension remains inside a hermetically closed vessel rotating
 191 at 5 rpm during one day before placing a sample on the rheometer plate
 192

193 III. RHEOLOGY IN THE ABSENCE OF MAGNETIC FIELD

194 A. Experimental results

195
 196 The rheogram of the suspension was obtained with an imposed stress rheometer MCR 502 from
 197 Anton-Paar. Most of the experiments were realized with a plate-plate geometry where both
 198 plates were covered with sandpaper of granulometry 40 µm to avoid slipping on the walls. The
 199 usual gap was 1mm and we must point that below 0.5mm, we have noticed that the critical
 200 shear stress was decreasing. In all the experiments, we take care that there is no spilling of the
 201 suspension, which can be the case at high stresses and/or high shear rates; if it was the case we
 202 have used the cylindrical Couette geometry with a small gap in order to prevent the migration
 203 of the particles from the higher shear rate domain close to the internal wall towards the external
 204 one.

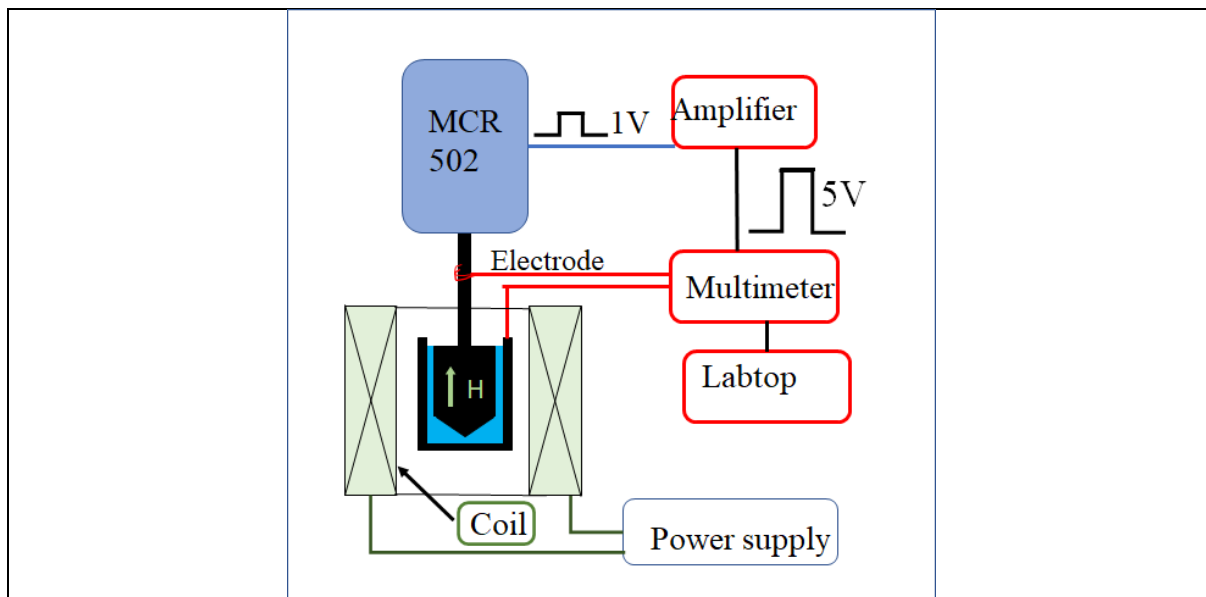


Fig.2 Sketch of the rheometer equipped with coils and devices to simultaneously record the resistance and the rheometric curves.

205
 206 The rheometer is equipped with a thermostated coil providing a magnetic field up to 65kA/m
 207 (corresponding to an induction $B \sim 0.08$ Tesla). When the measurement of the resistance is
 208 required, it is realized thanks to a brush of fine copper wires rubbing slightly on the axis of the
 209 tool. The extra torque due to this electrode is small (< 0.1 mN.m) and is subtracted from the
 210 viscous torque of the sample. The synchronisation between the measurements made by the
 211 software of the rheometer and the one of the resistance is done using the logical signal 0-1V
 212 sent by the hardware before each measurement to the logical gate of the multimeter Keithley
 213 2110 after amplification (cf. Fig. 2). The placement of the sample requires special care to relax
 214 the normal forces which are generated during the compression of the initial drop. For the last
 215 step of compression from $2\mu\text{m}$ to $1\mu\text{m}$, the descent speed is regulated between $1\mu\text{m/s}$ and $5\mu\text{m/s}$
 216 depending on the volume fractions, with a typical rotating speed of 0.1 rpm. For experiments
 217 with $\Phi \leq 0.66$, we finally get, at rest, a small negative normal force: $F_n \sim -0.1\text{N}$ (of the order of
 218 magnitude of the capillary force between the disk and the plate but well above the nominal
 219 resolution of 1mN), ensuring an absence of a residual compressive stress due to loading. A pre-
 220 shear was realized on all experiments with a ramp of stress from 0 to a stress below the critical
 221 one, typically 100Pa, which is then maintained constant during 3mn, followed by a rest time of
 222 30s at zero stress. Then a linear ramp of stress was applied, typically at a rate of 0.5 -1 Pa/s and
 223 with an acquisition rate of 1 or 2 points/s. For all the experiments the temperature was regulated
 224 at $T = 20^\circ\text{C}$ and a solvent trap was used
 225

226 In plate-plate geometry the shear rate is not constant and the stress versus shear rate curve must
 227 be corrected using the Mooney-Rabinovitch equation:

$$228 \quad \tau = \frac{\tau_a}{4} \left[3 + \frac{\dot{\gamma}}{\tau_a} \frac{d\tau_a}{d\dot{\gamma}} \right] \quad (4)$$

229 where τ_a is the shear stress given by the software of the rheometer. We have plotted in Fig.3
 230 the stress versus shear rate for an experiment made at a volume fraction $\Phi = 0.64$ in plate-plate
 231 geometry (black curve) and in cylindrical geometry (red curve). The first remarkable thing is
 232 that, in both geometries, we observe a sudden decrease of the shear rate by an order of
 233 magnitude at a critical point $(\dot{\gamma}_c, \sigma_c)$ and that above the critical point the shear rate oscillates
 234 about a constant value in the plate-plate geometry or with a slight increase in the case of the
 235 cylindrical geometry. For this volume fraction, we do not observe a second branch with a stable

236 flow up to the maximum stress we were able to use; here 3800 Pa in cylindrical geometry and
 237 only 1300 Pa in plate-plate geometry because, as can be seen in the Fig.3, it ends up with an
 238 expulsion of the liquid.

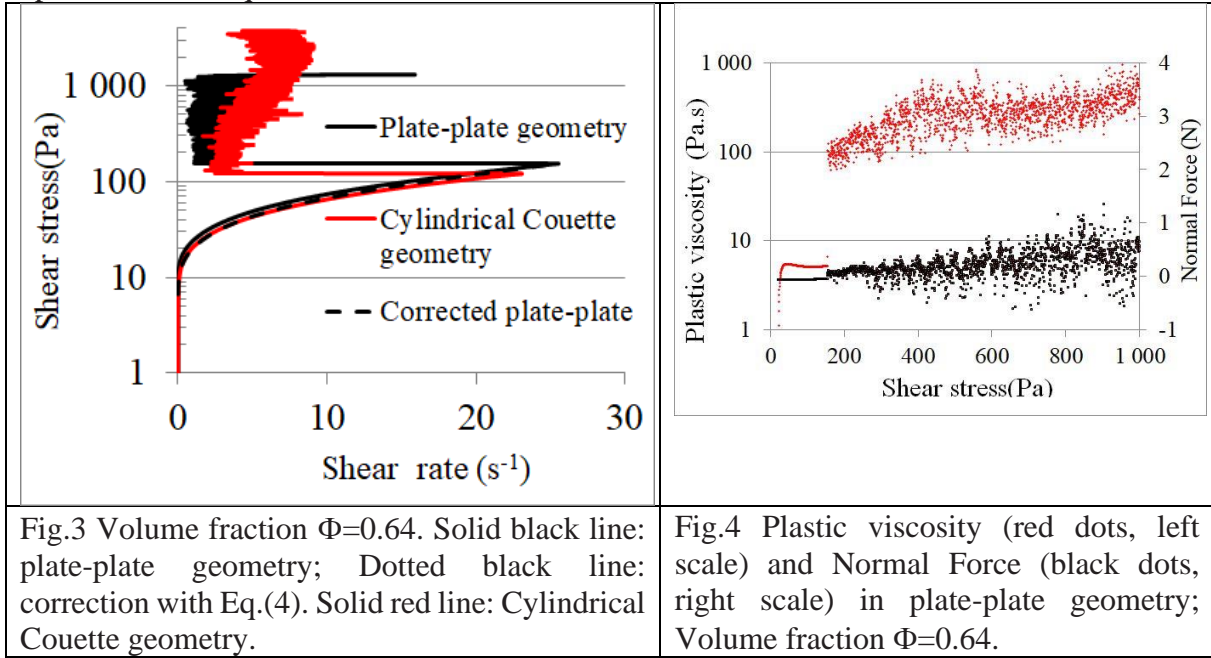


Fig.3 Volume fraction $\Phi=0.64$. Solid black line: plate-plate geometry; Dotted black line: correction with Eq.(4). Solid red line: Cylindrical Couette geometry.

Fig.4 Plastic viscosity (red dots, left scale) and Normal Force (black dots, right scale) in plate-plate geometry; Volume fraction $\Phi=0.64$.

239 The dotted line represents the application of Eq.(4) to the experimental curve below the critical
 240 stress. The experimental curve is first smoothed to calculate the derivative. We see that the
 241 corrected curve is lower than the experimental one and well follows the one obtained in
 242 cylindrical geometry below 10s^{-1} . After it begins to get closer to the initial curve, because the
 243 derivative $\frac{d\tau_a}{d\dot{\gamma}}$ is not constant but slightly increases as the suspension shear thickens when it
 244 approaches the jamming point. If the experimental curve was following a pure Bingham law
 245 with a yield stress τ_y^a and a plastic viscosity η_{pl} , then the corrected curve would have a true
 246 yield stress $\tau_y = \frac{3}{4}\tau_y^a$ and the same plastic viscosity. Then in this case the true critical stress
 247 obtained in plate-plate geometry would be simply $\tau_c = \tau_c^a - \tau_y^a/4$. Nevertheless, even a small
 248 shear thickening can give a quite different result, so for all the measurements made in plate-
 249 plate geometry we have used Eq.(4) to get the critical stress. In Fig.4 we have plotted the normal
 250 force and the plastic viscosity: $\eta_{pl} = (\tau - \tau_y)/\dot{\gamma}$ versus the stress. Below the jamming stress, the
 251 viscosity is almost constant: $\eta_{pl}=5.2\pm 0.2$ Pa.s and it jumps to $\eta_{pl}=90\pm 20$ Pa.s at the jamming
 252 point; at the same time, the normal force passes from slightly negative ($F_n = -0.06\pm 0.01\text{N}$) to
 253 positive ($F_n = -0.08\pm 0.02\text{N}$). Above the critical point both values increase with the stress and
 254 fluctuate a lot; nevertheless, as previously noted^{21,23}, the average stress on the upper plate :
 255 $F_n/\pi R^2$ remains proportional to the shear stress with, in our case, a coefficient of 0.29 ± 0.03 .
 256 Another important observation is that using different gaps in plate-plate geometry between
 257 0.5mm and 1.5 mm give the same result, which indicates that there is no noticeable slip on the
 258 plates. In the following we have used plate-plate geometry with a gap of 1mm or, when high
 259 shear rates are used for $\Phi < 0.62$, a cylindrical geometry. In Figs 5(a) and 5(b) we have gathered
 260 the shear stress versus shear rate curves obtained for volume fractions between $\Phi=0.53$ and
 261 $\Phi=0.67$. The curve for $\Phi=0.62$ is reported on both graphs : it is the volume fraction above which
 262 the critical stress of jamming σ_c steadily increases until the discontinuous jamming transition
 263 disappears at $\Phi=0.53$; also for $\Phi \leq 0.62$ the DST transition is accompanied by a sudden decrease
 264 of the shear rate followed by strong oscillations which are the signature of an instability
 265 described in detail for corn-starch suspensions⁴⁴ and explained by introducing the inertia of the
 266 rotating tool^{43,45}.

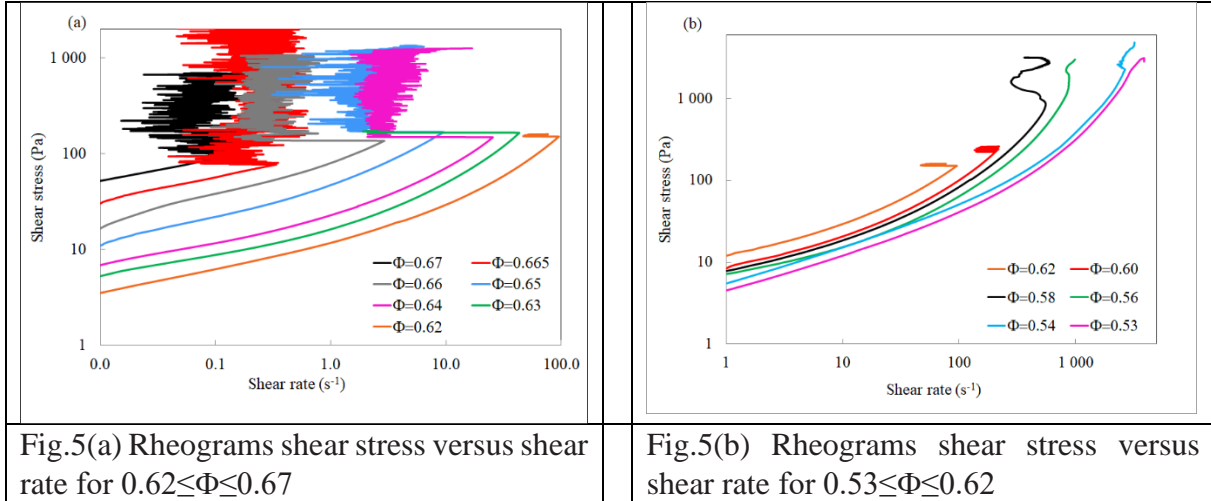


Fig.5(a) Rheograms shear stress versus shear rate for $0.62 \leq \Phi \leq 0.67$

Fig.5(b) Rheograms shear stress versus shear rate for $0.53 \leq \Phi \leq 0.62$

267 Another point that we want to emphasize is the fact that, even at the highest possible fraction:
 268 $\Phi=0.67$, after the DST transition we never observe a return to zero of the shear rate as predicted
 269 by the model of Wyart et Cates³² but rather an oscillating regime whose average value remains
 270 practically constant during the increase of the shear stress. This regime is shown in Fig.5(a) for
 271 $\Phi=0.66, 0.665, 0.67$ and in Fig.3 for $\Phi=0.64$. A similar behaviour was reported for other kinds
 272 of suspensions e.g. corn-starch^{44,46}, submicronic PMMA suspensions stabilized with grafted
 273 polymers^{9,14}, polystyrene particles of diameter $0.3\mu\text{m}$ ²¹, silica¹⁵ and alumina particles of
 274 micronic size in water at different pH. This behaviour with a shear rate fluctuating around a
 275 constant value above the critical shear stress in stress-controlled experiments seems quite
 276 generic and can't be explained by the Wyart-Cates model. We shall come back to this point at
 277 the end of this section (sub-section C). In the following figures we have plotted the plastic
 278 viscosity obtained from a fit of the linear part of the curve by a Bingham law $\eta(\dot{\gamma}) = \tau_y + \eta_{pl}\dot{\gamma}$
 279 versus the effective volume fraction given by Eq.(3).

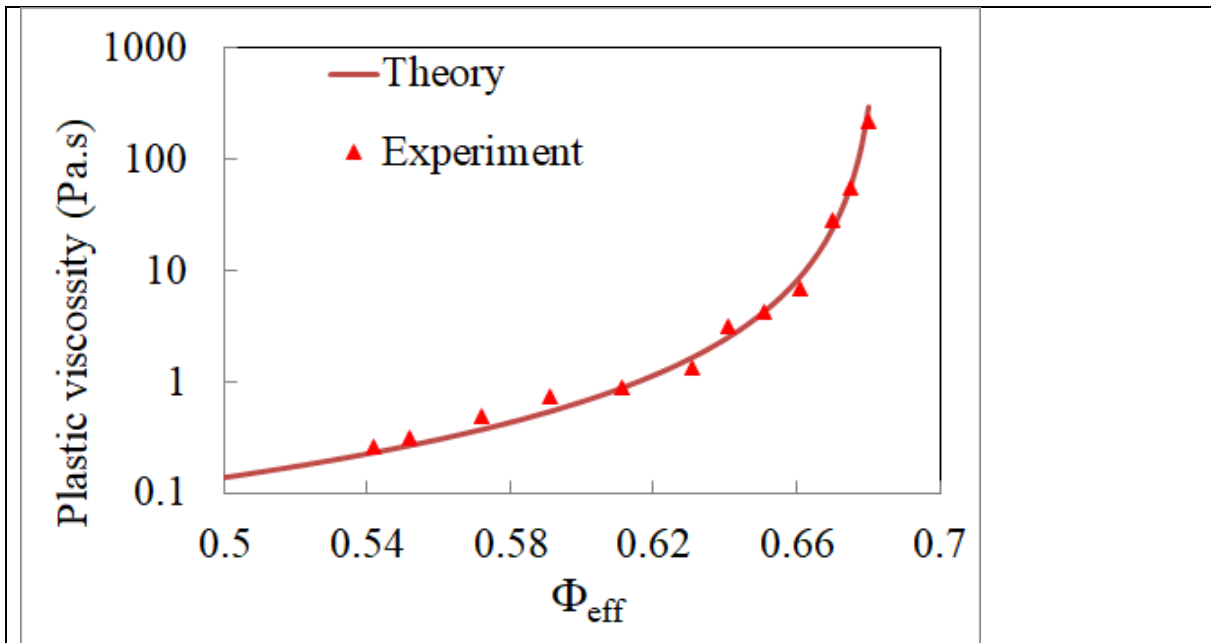
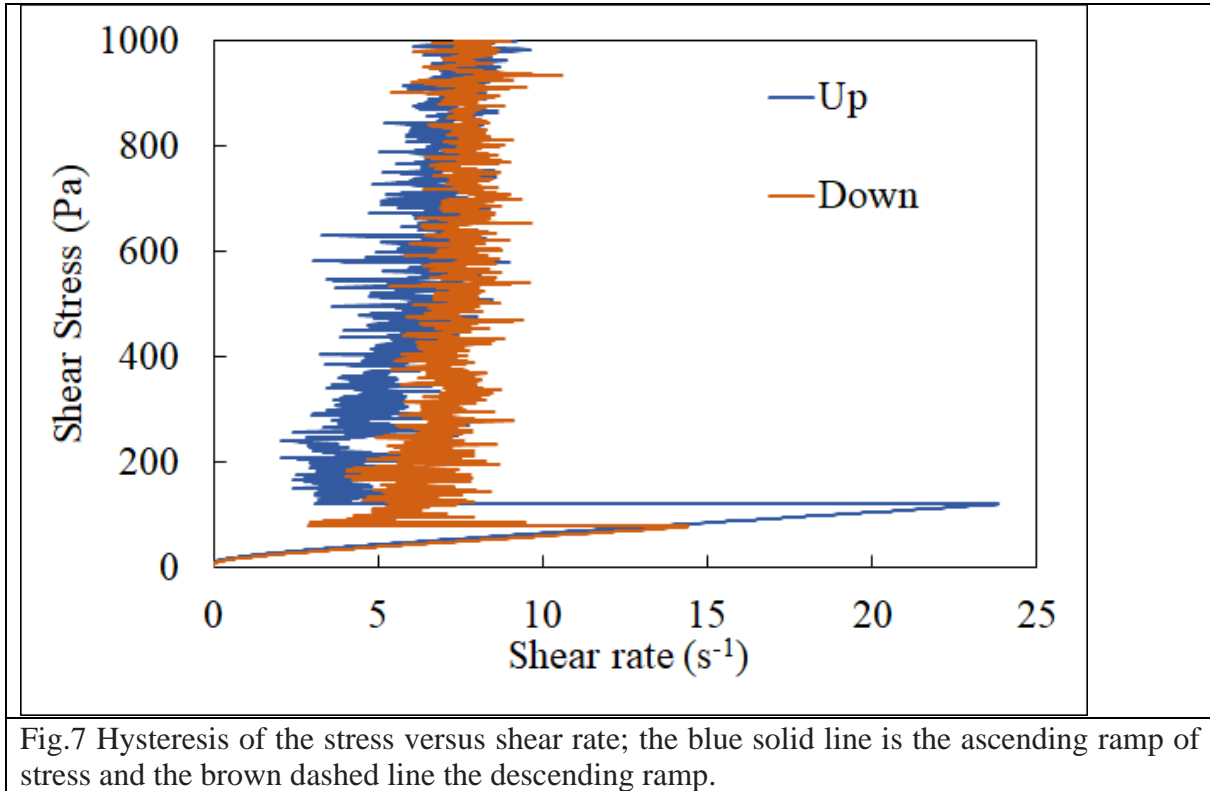


Fig.6 Plastic viscosity versus the volume fraction: $\eta_{pl}(\Phi_{eff}) = A(1 - \frac{\Phi_{eff}}{\Phi_{0eff}})^{-2}$ With $A=0.01$ Pa.s and $\Phi_{0eff}=0.684$.

280 The value $\Phi_{\text{eff}}=0.684$ given by the fit is very close to the prediction obtained from the use of
281 the equivalence with a bidisperse suspension (cf Appendix A) and we shall keep it for the
282 analysis of the rheological model.

283 Before trying to explain the experimental curves with the help of a rheological model we also
284 want to mention that all the curves presented are taken during the first rise of stress or shear
285 rate (in rate control experiments) after loading the suspension. As can be seen in Fig.7, the

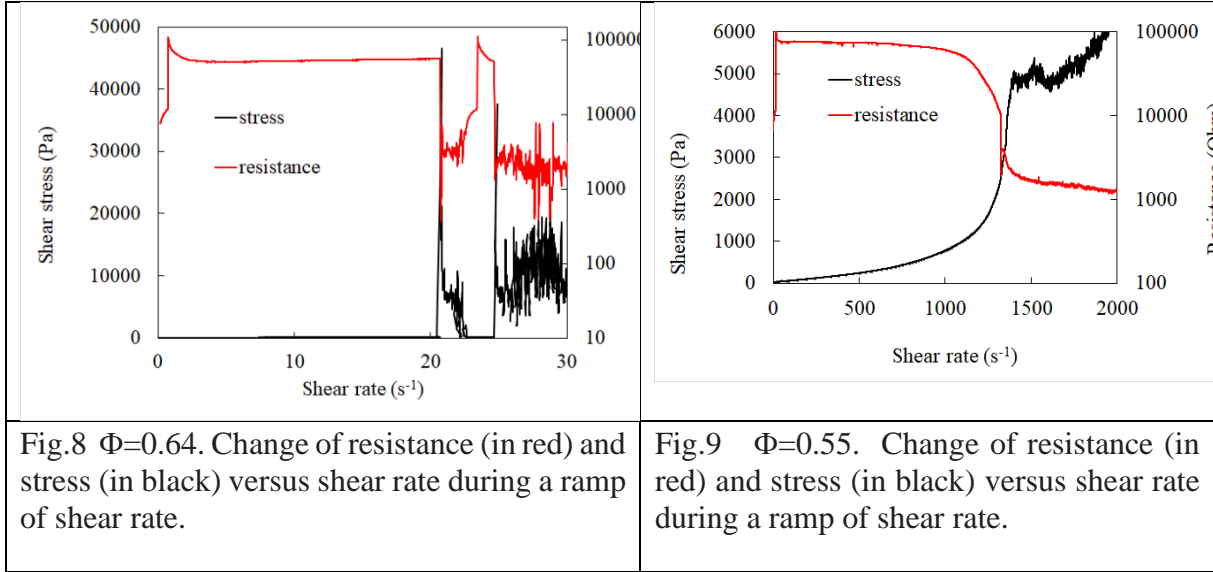


286

287 descending curve (brown dashed line) shows a hysteresis and falls on the ascending one at a
288 lower stress, but after that, remains on the ascending one, showing that the suspension has
289 recovered its equilibrium state. This hysteresis can be much more important when the DST
290 transition occurs at high stresses as is the case at volume fraction lower than 0.62. In this case
291 a second ramp of stress with the same suspension gives a higher viscosity on the descending
292 branch, which is the signature of an irreversible aggregation induced by the preceding high
293 stress. The initial state can nevertheless be recovered by a pre-shear at an intermediate stress.

294 The fact that the DST transition is provoked by a percolation of frictional contacts between
295 particles has been demonstrated by numerical simulation²⁷ but to our knowledge there is no
296 experimental demonstration of the correlation between the percolation of contact forces and the
297 DST transition. In our suspension we are using coated iron particles and this coating increases
298 the resistivity of the suspension. If, on the other hand, the DST transition is related to the
299 formation of a percolated network of frictional contacts, it means that the coating has been
300 removed and the transition should manifest through a decrease of the conductivity of the
301 suspension. The resistance between the two plates or between the outside cylinder and the bob
302 was measured using a comb of thin conductive wires rubbing on the shaft. We have presented
303 in Fig.8 and Fig.9 the change of the resistance of the suspension associated with the DST
304 transition respectively for a volume fraction $\Phi=0.64$ in the domain where there is a strong

305 decrease of the shear rate and for $\Phi=0.55$ which is close to the lower limit of the DST transition.
 306 Both measurements are made in an imposed shear rate ramp in cylindrical Couette geometry
 307 where high stresses are accessible without the expulsion of the suspension contrary to plate-
 308 plate geometry. At $\Phi=0.64$ we have imposed a ramp of shear rate, and before the definitive
 309 transition at $\dot{\gamma}=24\text{ s}^{-1}$, we see a transient exploration of the high stress domain accompanied by
 310 a sudden drop of the resistance which is the negative footprint of the stress jump. The drop of
 311 the resistance and the jump of shear stress are very well correlated in both cases. The effective
 312 surface of contact between the particles is difficult to quantify because a part of the conductivity
 313 can be due to tunnel effect⁴⁷. Nevertheless, this sudden decrease of resistance is an experimental
 314 proof of the formation of a percolation network of frictional contacts between the particles.



315 For a lower volume fraction, $\Phi=0.55$, the change of resistance as well as the change of stress
 316 during a ramp of shear rate is much softer but, in total, is of the same order of magnitude. We
 317 can also note that at the beginning of the shear there is an increase of the resistance, which is
 318 due to the resuspension of the particles and to the destruction of a fragile network which was
 319 formed at the bottom of the cylinder in the presence of sedimentation. Besides the experimental
 320 proof of the presence of frictional contacts between particles this experiment also shows that
 321 the formation of this network can be either progressive at the lower volume fraction or very
 322 abrupt at higher volume fraction. We shall come back to this point in the next section

323

324 B. Comparison with Wyart-Cates model

325 The discontinuous shear thickening transition is characterized by a point in the rheogram $\sigma =$
 326 $f(\dot{\gamma})$ where the derivative $\frac{d\dot{\gamma}}{d\sigma} = 0$. As $\dot{\gamma} = \sigma/\eta(\sigma)$, taking the derivative gives the condition: $\beta =$
 327 $\frac{d\text{Log}(\eta)}{d\text{Log}(\sigma)} = 1$ which is often used in the plot $\eta = f(\sigma)$ in Log-Log scale to characterize the DST
 328 transition.

329 In the model of Wyart and Cates³² the viscosity can diverge at a volume fraction lower than Φ_0
 330 called Φ_j^μ . In granular materials, the minimum volume fraction which can support a stress is
 331 known as the random loose packing, $\Phi_{RLP} \sim 0.55-0.56$ for monodisperse spheres, so it seems
 332 reasonable to think that $\Phi_j^\mu \neq \Phi_{RLP}$. The following linear relation is taken in the W-C. model for
 333 the dependence of the jamming volume fraction to $f(\sigma_r)$ where $\sigma_r = \sigma/\sigma_c$:

334 $\Phi_j(f) = \Phi_j^\mu f + \Phi_0(1 - f)$ where $f = f(\sigma_r)$ with $0 < f < 1$ (5)

335 The divergence of the relative viscosity at Φ_j is then supposed to follow the same law than for
 336 frictionless spheres with $\Phi_j(f)$ replacing Φ_0 :

337 $\eta_r(\Phi) \propto (\Phi_j(f) - \Phi_{eff})^{-2}$ or $\eta_r(\Phi) \propto \left(1 - \frac{\Phi_{eff}}{\Phi_j(f)}\right)^{-2}$ (6)

338 The second expression is equivalent, close to the divergence, but is more usual in rheology so
 339 we shall keep it in the following. The power -2 was shown to well represent experimentally the
 340 divergence of the viscosity at the vicinity of the jamming volume fraction^{49,50} and is also
 341 compatible with numerical simulations whatever the value of the friction coefficient^{28,51,52}.
 342 When the stress and so $f(\sigma_r)$ increases, $\Phi_j(f)$ decreases and can reach the actual value of Φ if
 343 $\Phi_j^\mu < \Phi < \Phi_0$, then the viscosity diverges and the flow should stop. In a range of volume fraction
 344 below Φ_j^μ there is still a domain of stress where the DST transition subsists but do not lead to a
 345 jammed situation. A phase diagram in the plane (σ, Φ) illustrating these different behaviour can
 346 be found in A.Singh *et al*²⁸. In the W-C. paper the function $f(\sigma_r)$ was chosen arbitrary as $f(\sigma_r)$
 347 $= 1 - \exp(-\sigma_r)$. In a recent paper R. Radhakrishnan *et al*⁵² the authors have calculated the function
 348 $f(\sigma_r)$ from the distribution of normal forces between particles: $P(\theta)$ with $\theta = F_n / \langle F_n \rangle$ and:

349
$$f(\theta^*) = \frac{\int_{\theta^*}^{\infty} P(\theta) d\theta}{\int_0^{\infty} P(\theta) d\theta}$$
 (7)

350 The average value of the normal force should be proportional to the applied stress σ so
 351 $\theta^* = \frac{\lambda \sigma_c}{\sigma} = \lambda / \sigma_r$ where $\lambda = 1.85$ was a proportionality constant found numerically to be
 352 independent of the volume fraction. We have plotted in Fig.10 a curve representing the values
 353 they have obtained by numerical simulation in the low friction limit ($\mu = 10^{-4}$) and a fit by the
 354 function:

355 $f(\sigma_r) = e^{-\left(\frac{\lambda}{\sigma_r}\right)^q}$ with the parameters $\lambda = 1.712$ and $q = 1.163$ (8)

356 The parameter λ shifts the curves since it scales $\sigma_r = \sigma / \sigma_c$ and should not depend too much on the
 357 volume fraction since the characteristic magnitude of the repulsive force does not depend on
 358 the volume fraction; the parameter, q , modifies the sharpness of the transition. On the other
 359 hand, as shown in this last paper, the function $f(\sigma_r)$ is quite insensitive to the value of μ .

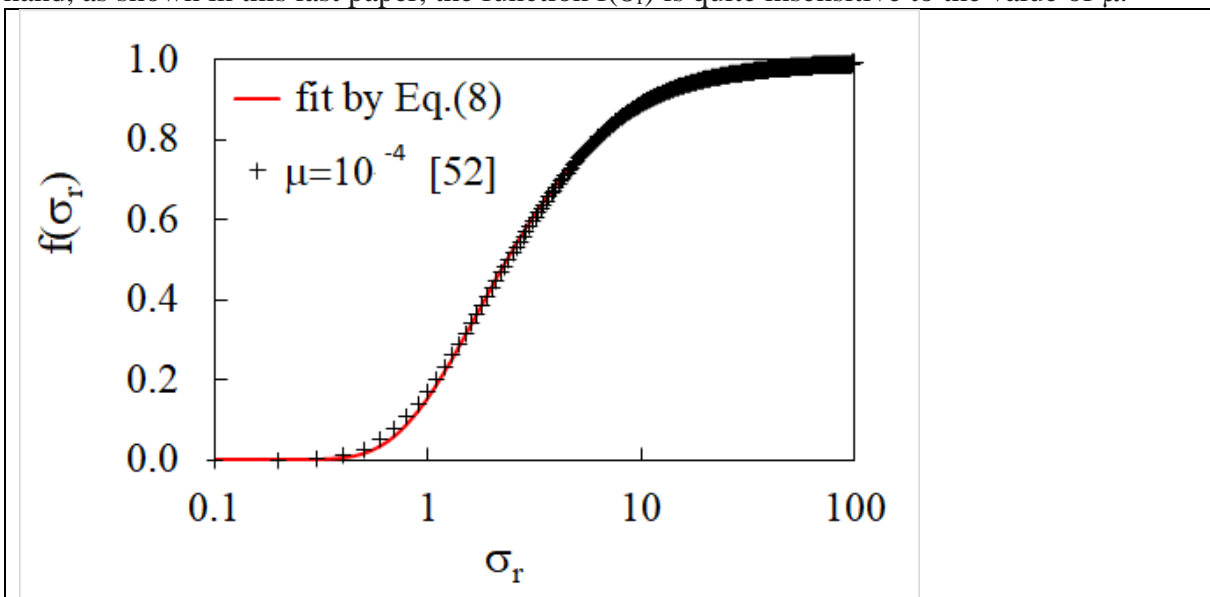


Fig.10 Fit of the values of $f(\sigma_r)$ for $\mu = 10^{-4}$ (R. Radhakrishnan *et al.*⁵²) with Eq.(8) and $\lambda = 1.712$; $q = 1.163$

360 Furthermore Eq.(8) for $f(\sigma_r)$ was previously used ^{28,53} to represent the data obtained from
 361 numerical simulations. It is also possible to use a prefactor in Eq.(8): $f_{\max}(\Phi)$ ⁵⁴, but at the cost
 362 of a supplementary parameter which will not be useful to interpret our experimental data.

363 In order to fit the dependence of the viscosity versus the volume fraction for different values of
 364 the friction coefficient Singh *et al* ²⁸, have proposed to generalize Eq.(6) to take into account
 365 the variation of the viscosity with the friction coefficient. Their modification is the following:

$$366 \quad \eta_c(\Phi, \sigma_r) = \alpha(\sigma_r, \mu) \left(1 - \frac{\Phi_{eff}}{\Phi_j(\sigma_r, \mu)}\right)^{-2} \quad (9)$$

367 Where the function α has the dimension of a viscosity with:

$$368 \quad \alpha(\sigma_r, \mu) = \alpha_\mu f(\sigma_r) + \alpha_0(1 - f(\sigma_r)) \quad (10)$$

$$369 \quad \text{and } \Phi_j(\sigma_r, \mu) = \Phi_j^\mu f(\sigma_r) + \Phi_0(1 - f(\sigma_r)) \quad (11)$$

370

371 The parameters α_μ and Φ_j^μ are functions of the friction coefficient, μ , and are obtained from a
 372 fit of the numerical results with an empirical function. Wagner *et al.* ³³ have used their
 373 prediction for these functions together with experimentally determined values of the friction
 374 coefficient in order to compare the predictions of the model with some experimental results on
 375 several kind of suspensions. They found strong deviations between the model and their
 376 experimental results.

377 The coefficient, α_0 , corresponds to the low stress range: $f(\sigma_r) \sim 0$ and is related to the beginning
 378 of the experimental curve $\sigma(\dot{\gamma})$. The second parameter α_μ is a fitting parameter without real
 379 physical significance, so we shall discard it and take:

$$380 \quad \alpha(\sigma_r, \mu) = \alpha_0 \quad (12)$$

381

382 In our system the coating molecule is a superplasticizer playing the role of a polymer brush at
 383 the surface of the particles and we have seen that the divergence of the low stress viscosity
 384 versus the volume fraction, (Fig.6), was corresponding to the theoretical random close packing
 385 of our polydisperse suspension (cf Appendix A). It means that the friction coefficient is close
 386 to zero. This agrees with measurements^{55,56} made with a surface force balance on mica surfaces
 387 covered by PEO polymer of similar length where the friction coefficient was of order 10^{-3} . In
 388 the model we need also to know the lower jamming volume fraction Φ_j^μ . In principle it can be
 389 determined from the viscosity of the second branch of $\eta_c(\sigma_r)$ in the domain of DST where
 390 $\Phi < \Phi_j^\mu$ for large values of σ_r where $f(\sigma_r) \rightarrow 1$, since in this case η_c becomes a constant
 391 independent of the stress (cf. Eqs. (9)-(11)). In this zone -typically for $\phi \leq 0.58$ - there is a second
 392 branch, but due to high stresses and shear rates it is not possible to obtain a reproducible value
 393 of the viscosity, cf. Fig.5(b). In the W-C model and in numerical simulations the friction
 394 coefficient μ is supposed to be independent of the shear stress but in practice, and in the
 395 presence of a layer of adsorbed polymer at the surface of the particles, we expect that the friction
 396 increases with the stress due an increase of the entanglement between the polymers. It was
 397 already observed by AFM measurements where the friction increases a lot due either to the
 398 entanglement of the polymer or even to their expulsion from the surface ^{56,57}. In this context it
 399 is reasonable to suppose that Φ_j^μ corresponds to the loose random packing at high friction ($\mu > 1$).
 400 For monodisperse spheres, several authors ^{52,58,59} have found: $\Phi_j^\mu \sim 0.55-0.56$ which is also close
 401 to the high friction limit obtained by numerical simulation with the critical load model ²⁸. We
 402 have transposed these values to a bidisperse suspension using the same methods as for Φ_{RCP} (
 403 cf. Appendix A) and we have obtained $\Phi_j^\mu = 0.59 \pm 0.01$. Finally, to check the model we shall
 404 use the following values: $\Phi_0 = 0.684$ and $\Phi_j^\mu = 0.59$. In any event, we shall see that even a
 405 change of ± 0.01 in Φ_j^μ does not change our conclusions.

406 Besides these two volume fractions, the other parameters of the model are those, λ , q , defining
 407 the fraction of frictional contacts (Eq.(8)) and the coefficient α_0 . The—coefficient, α_0 ,
 408 corresponds to the low stress range: $f(\sigma_r) \sim 0$ and is related to the beginning of the experimental
 409 curve $\sigma(\dot{\gamma})$ which can be represented either by a Bingham model or more generally by a
 410 Herschel-Buckley(HB) model: $\sigma = \tau_y + K \cdot \dot{\gamma}^p$.

411 In our experiments with high volume fraction, we have a yield stress which is not negligible.
 412 We follow the analysis made in Singh *et al.* ⁶⁰. They found that the total viscosity was well
 413 represented by adding the Herchel-Buckley viscosity at low stress and the contact viscosity
 414 (Eq.(9)) at high stress. In this approach, the beginning of the contribution of the contact
 415 viscosity depends strongly on the exponent, p , of the HB law. Since in the experiment we do
 416 not have access to the contact viscosity we adopt the view that we are not looking for a good
 417 model of the low stress behaviour but rather to the application of the W-C model at intermediate
 418 and high stress. To reduce the number of parameters, instead of the HB law, we have used the
 419 Bingham one even if it does not fit very well the lower part of the stress versus shear rate curve.
 420 So, we shall write:

$$421 \quad \sigma = \tau_y + (\eta_B + \eta_c(\sigma))\dot{\gamma} \quad \text{with} \quad \eta_c(\sigma) = \alpha_0 \left(1 - \frac{\Phi_{eff}}{\Phi_j(\sigma_r)}\right)^{-2} \quad (13)$$

422 In this description η_B is the plastic viscosity obtained by fitting the beginning of the curve by a
 423 Bingham law and we suppose that all the shear thickening part is described by the W-C model
 424 represented by the contact viscosity η_c . On the other hand we have $\eta_c(\sigma \rightarrow 0) =$
 425 $\alpha_0 \left(1 - \frac{\Phi_{eff}}{\Phi_0}\right)^{-2}$, since $f(\sigma_r) \sim 0$. Then we can just incorporate η_B in η_c by imposing that the
 426 value of α_0 gives back η_B when Φ_j tends to Φ_0 at low stress. Finally, we end up with:

$$427 \quad \sigma = \tau_y + \eta_{pl}(f(\sigma))\dot{\gamma} \quad ; \quad \eta_{pl}(f(\sigma)) = \alpha_0 \left(1 - \frac{\Phi_{eff}}{\Phi_j(f(\sigma_r))}\right)^{-2} ; \quad \alpha_0 = \eta_B \left(1 - \frac{\Phi_{eff}}{\Phi_0}\right)^{+2} \quad (14)$$

428
 429 In Eq.(14) the only remaining parameters are those (λ, q) defining the function $f(\sigma_r)$ (cf Eq.(8)).
 430 They can be determined directly by the condition that the theoretical curve should pass through
 431 the transition point $(\sigma_c, \dot{\gamma}_c)$:

$$432 \quad \sigma_c - \tau_y = \eta_{pl}(\sigma_c)\dot{\gamma}_c \quad \text{and} \quad \left. \frac{d\dot{\gamma}}{d\sigma} \right|_{\sigma=\sigma_c} = 0 \quad (15)$$

433 Or equivalently, using $\dot{\gamma}_c = (\sigma_c - \tau_y)/\eta_{pl}(\sigma_c)$, where $\eta_{pl}(\sigma)$ is given by Eq.(14) we end up
 434 with the two equations:

$$436 \quad \frac{\sigma_c - \tau_y}{\dot{\gamma}_c} = \eta_{pl}(\sigma_r = 1) \quad (16)$$

$$437 \quad 1 = \frac{\sigma_c - \tau_y}{\eta(\sigma_c)} \left[\left. \frac{d\eta_{pl}(\sigma)}{d\sigma} \right|_{\sigma=\sigma_c} \right] \quad (17)$$

438 The results are shown in Figs 11-12 for the volume fractions $\Phi=0.58, \Phi=0.64$ and $\Phi=0.66$. The
 439 parameters used to obtain these curves are listed in table 1. The two first parameters are those
 440 of the Bingham law (τ_y, η_B) representing the part of the curve which is not shear thickening.
 441 The third one α_0 is obtained from η_B (Eq.(14)), then λ and q characterize the function $f(\sigma)$ and
 442 the last quantity $f(\sigma_c)$ is the proportion of frictional contacts at the critical stress as obtained
 443 from the values of λ and q reported in Eq.(8) for $\sigma_r=1$. For $\Phi=0.58$ the experiment was done in
 444 cylindrical Couette rheometry, whereas for $\Phi=0.64$ and $\Phi=0.66$ the experiments were done in
 445 plate-plate geometries. For this last geometry the experimental curves presented in Figs.12(a)
 446 and Fig.12(b) have been corrected as described by Eq.(4) and illustrated in Fig.3. In Fig.11 we
 447 have presented the results for $\Phi=0.58$.

448
 449

Φ	$\tau_y(\text{Pa})$	η_B	α_0	λ	q	$f(\sigma_c)$
0.58	2.1	0.81	0.018	1.08	1.19	0.335
0.64	18.4	4.92	0.020	1.46	3.50	0.023
0.66	40.1	28.5	0.034	1.02	111	$3.3 \cdot 10^{-4}$

Table 1 Parameters used in the Wyart Cates model for the volume fractions $\Phi=0.58,0.64,0.66$

450

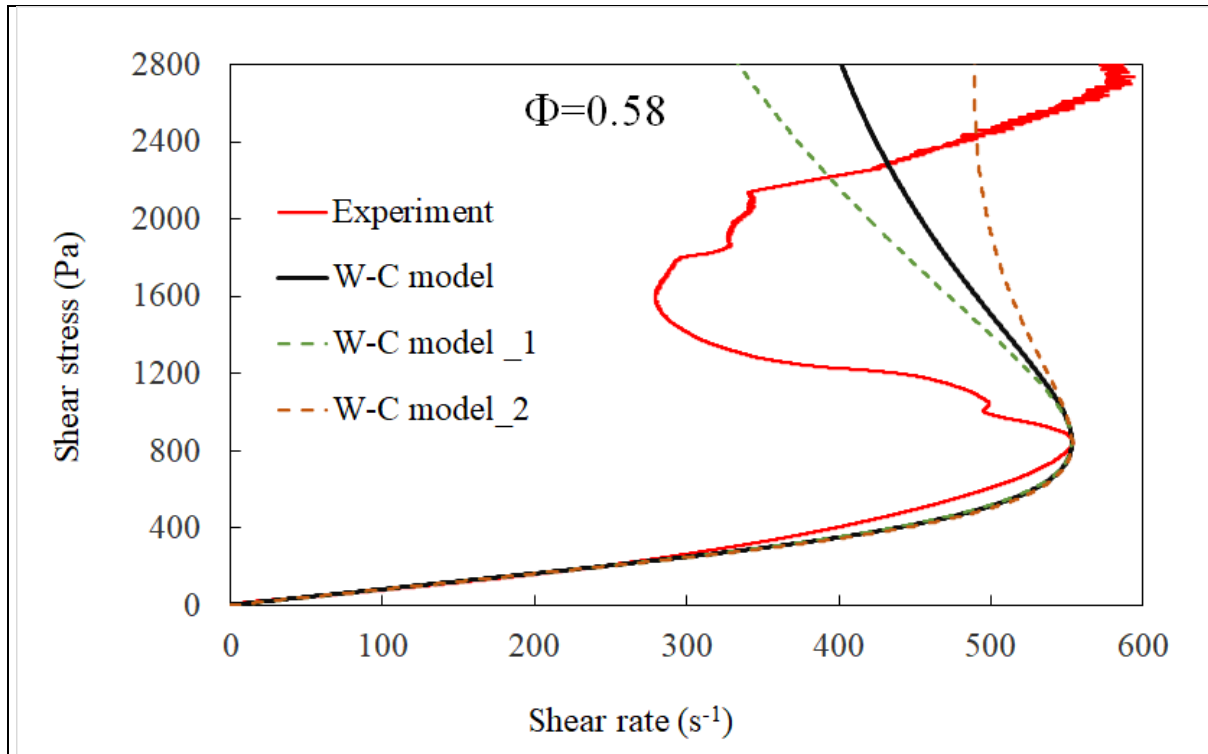
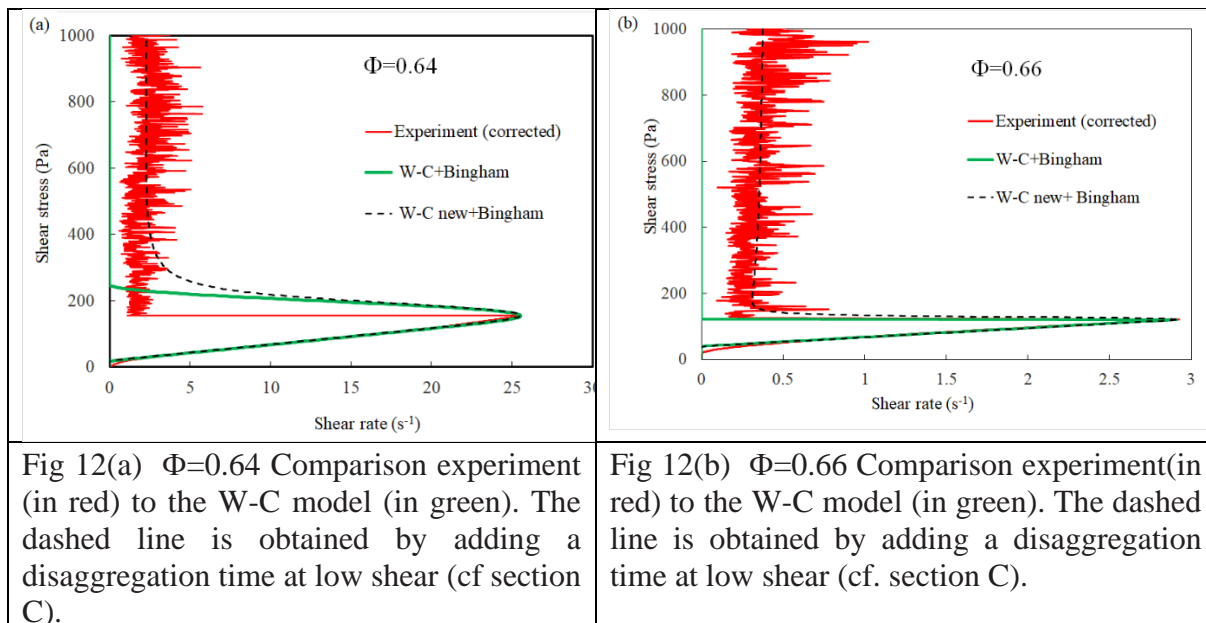


Fig.11 $\Phi=0.58$ Comparison of the experimental curve (in red) to the theoretical one (in black) with $\Phi_j^\mu = 0.59$. The dashed curve in green corresponds to $\Phi_j^\mu = 0.58$ and the one in brown to $\Phi_j^\mu = 0.60$

451 The red curve is the experimental one, the black one is the theoretical one (obtained from a fit
452 of the beginning of the curve ($\dot{\gamma} < 200 \text{ s}^{-1}$) by a Bingham law, The resulting curve does not fit
453 the experimental one very well below the critical point and not at all above. The turning point
454 corresponding to the S shape (not represented here) is found at $\sigma \sim 6000 \text{ Pa}$ instead of about
455 1600 Pa experimentally. It is worth noting that adding the parameter α_μ (Eq.(10) in the prefactor
456 of the viscosity) does not improve significantly the agreement between the experiment and the
457 model. On the other hand, this discrepancy can't be attributed to the uncertainty on Φ_j^μ as can
458 be seen on Fig.11 where the two curves with $\Phi_j^\mu = 0.58$ and $\Phi_j^\mu = 0.60$ are still far from the
459 experimental one.
460



461
 462 The results for the volume fractions $\Phi=0.64$ and $\Phi=0.66$ are presented in Figs.12(a) and 12(b).
 463 For the moment we discard the dotted lines which will be discussed later. For $\Phi=0.64$ we see
 464 in the linear scale that we are close to a pure Bingham behaviour but, there is a small shear
 465 thickening before the transition. The value $q=3.50$ (cf Table 1) indicates that the transition is
 466 more abrupt than at $\Phi=0.58$ where $q=1.19$ -(close to the value $q=1.16$ of the numerical
 467 simulation of Fig.10). On the contrary at $\Phi=0.66$ we have a transition which occurs without
 468 being preceded by shear thickening. A fit of the upper part of the curve by a Bingham law well
 469 represents the experimental behaviour above 0.5 s^{-1} , cf. Fig.12(b). As there is no shear
 470 thickening before the transition, it amounts to say that the percolating network of frictional
 471 contacts is created suddenly at $\sigma=\sigma_c$, what is reflected by the huge value $q=111$.

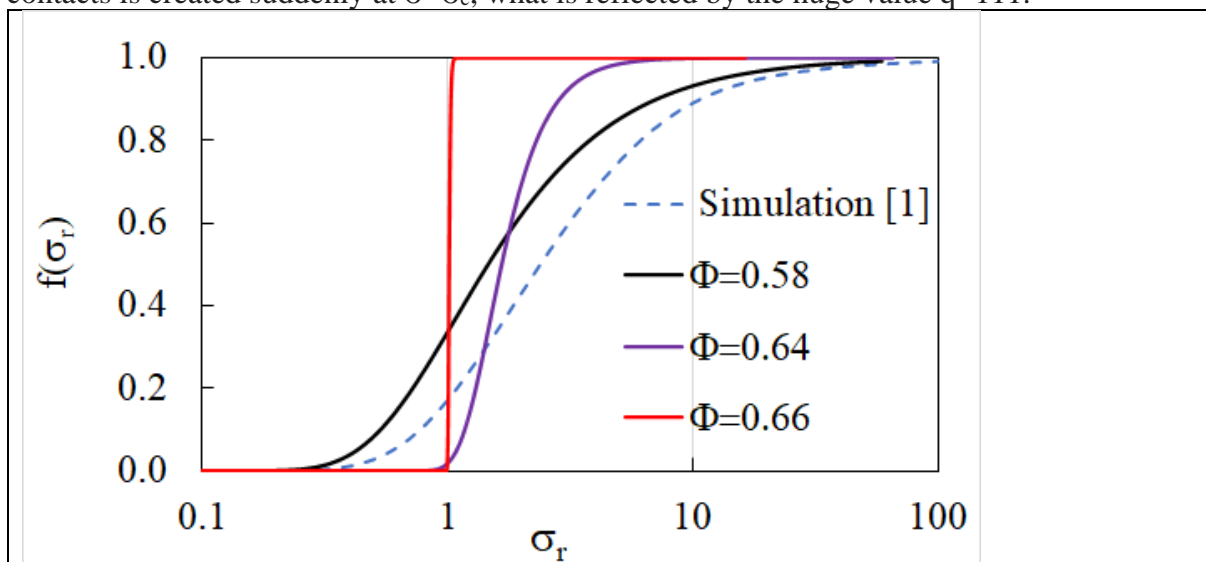


Fig.13 Evolution of the fraction of frictional contacts for different volume fractions with the relative stress $\sigma_r=\sigma/\sigma_c$. The dashed line refers to the result of numerical simulation which does not depend on volume fraction (Radhakrishnan *et al.*⁵², Mari *et al.*²⁷). The other curves come from the the Wyart-Cates theory with conditions given by Eqs.(14)-(17)

472

473 Said differently, the function $f(\sigma_r)$ jumps from 0 to 1 at $\sigma=\sigma_c$. We have plotted in Fig.13 the
474 evolution of this function with the stress. We see that at $\Phi=0.58$, the progressive increase of
475 $f(\sigma_r)$ is like the one observed in numerical simulation but with a shift relatively to σ_r . This shift
476 is not surprising since the value of λ depends on the specific shape of the repulsive barrier
477 preventing the particles to come into contact.

478 The fact that there is only a small shear thickening before the transition at $\Phi=0.64$ is translated
479 by a sharper evolution of the function $f(\sigma_r)$, and finally we have the step function at $\Phi=0.66$.

480 This evolution of $f(\sigma_r)$ with the volume fraction is supported by the measurement of the
481 resistance versus the stress, Figs 8 and 9, which shows qualitatively the same difference of
482 behaviour between the volume fraction $\Phi=0.64$ where the drop of resistance is abrupt and
483 $\Phi=0.55$ where it is much more progressive. It is worth pointing again that this drop of resistance
484 at the DST transition is an experimental signature of the formation of a percolating network of
485 frictional contacts. The fact that, contrary to the simulation results, the fraction of frictional
486 contacts for the same stress depends strongly on the volume fraction, is likely due to the
487 complexity of the interaction between the layers of adsorbed polymers. We indeed expect that,
488 for the same shear stress, the interpenetrating zone will increase with the volume fraction,
489 giving more efficiency to the applied stress for removing the layer of adsorbed polymer.

490

491

492 C. The absence of jamming above the DST transition

493

494 In the W-C model the suspension should stop to flow above a given stress if the volume fraction
495 is between Φ_0 and Φ_j^u because, in this range, the jamming volume fraction $\Phi_j(\sigma)$ will always
496 reach the actual volume fraction Φ when the stress increases, causing the divergence of the
497 viscosity. In practice we see (cf. Figs 12(a) and 12(b)) that, instead of going to zero, the shear
498 rate keeps, in average, an almost constant value when the stress is increased above the DST
499 transition. As pointed out when discussing the results presented in Fig.5, many authors already
500 noticed this kind of behaviour on different kinds of suspensions. One could object that this
501 residual shear rate is due to some slipping of the suspension on the walls, but on the other hand
502 if we apply a magnetic field of about 100kA/m to the same suspension of carbonyl iron particles,
503 it will show a yield stress of several kPa without any slipping in the same plate-plate geometry
504 ^{61,62}. Besides, the role of the inertia of the rotating tool was recognized to play a major role in
505 the instability which occurs when the differential viscosity is negative ^{43,45,63,64}. When coupled
506 to the W-C model, the introduction of an exponential relaxation for the time evolution of $f(t)$
507 towards its equilibrium value $f(\sigma_r)$, allows to well recover the oscillations above the transition
508 but did not explain the persistence of these oscillations at stresses where the W-C model predicts
509 the total stop of the flow. By adding in the time evolution of $f(t)$ a second term: $H(f_m-f)$ allowing
510 the growth of $f(t)$ with the shear rate, it is possible to obtain an asymptotic value of the shear
511 rate at high shear stress ⁶⁵ but at the condition to take $H \propto \sigma^{3/2}$ which seems rather arbitrary.
512 In a recent paper on DST in capillary flow ⁶⁶ we have proposed another explanation and a
513 modification of the W-C model which well succeeded to reproduce this non-zero -almost
514 constant- shear rate at high stresses. Our approach was based on the idea that a state of flow
515 arrest at high stress, which would be only due to friction and not to adhesive forces, should be
516 unstable. This is because, in the absence of flow and of large enough adhesive forces, the
517 entropic forces, like those due to a small residual Brownian motion or to a change of
518 configuration of the coating molecules present on or around the surfaces, will be strong enough
519 to destroy some fragile links in the network of frictional contacts leading to a restart of the flow.
520 This mechanism will give, on average, a non-zero shear flow at high stresses, and can be simply
521 taken into account by inserting the condition that the fraction of frictional contacts should

522 progressively vanish if the shear rate tends to zero, whatever the value of the stress. This can
 523 be done for instance by multiplying the function $f(\sigma_r)$ (Eq.(8)) by a function g , of the shear rate
 524 which vanishes at zero shear rate and tends to unity when it increases:

$$525 \quad f'(\sigma_r, \dot{\gamma}) = f(\sigma_r) * g(t_d \cdot \dot{\gamma}) \quad (17)$$

526 where t_d is a parameter related to the rupture time of the frictional contacts. We previously took
 527 arbitrarily a Langevin function for the function g ⁶⁶, but the precise shape of this function can
 528 be deduced from an evolution equation of the function $f(t)$ which is a structural parameter like
 529 others often used to describe the time dependent rheology. Such an approach combines two
 530 mechanisms, one for the building of the structure and the other for its destruction². In this way,
 531 we will write:

$$532 \quad \frac{\partial f}{\partial t} = -\frac{1}{t_B} (f(t) - f(\sigma_r)) - \frac{f(t)}{t_d} \quad (18)$$

533 The first term describes the relaxation of the structure to its equilibrium value corresponding to
 534 the stress σ_r , given by Eq.(8) and was already used to reproduce the oscillations of the shear
 535 rate above the transition⁴². If the fraction of frictional contacts is below its equilibrium value,
 536 it will rise with a characteristic time t_B which will be inversely proportional to the collision rate
 537 and so to the shear rate: $t_B = 1/(\dot{\gamma} C_B)$ where C_B is a constant. On the other hand, in the absence
 538 of shear, we expect that the frictional contacts will be destroyed with a characteristic time t_d
 539 that, for simplicity, we suppose independent of the stress. At equilibrium $\frac{\partial f}{\partial t} = 0$ and from
 540 Eq.(18) we have:

$$541 \quad f'_{eq}(\sigma_r, \dot{\gamma}) = f_{eq}(\sigma_r) \frac{\dot{\gamma}}{\frac{1}{t_d \cdot C_B} + \dot{\gamma}} = f_{eq}(\sigma_r) g(\dot{\gamma}) \quad (19)$$

542 In Eq.(19) we have added the subscript “eq” to emphasize that it is the equilibrium value. Now
 543 the jamming volume fraction depends also on the shear rate since f is replaced by f' in Eq.(11).
 544 At high value of σ_r we have $f_{eq}(\sigma_r) \rightarrow 1$ then $\Phi_j \rightarrow (1-g(\dot{\gamma}))\Phi_0 + g(\dot{\gamma})\Phi_m$ and we end up
 545 with:

$$546 \quad \eta \rightarrow \frac{1}{(\Phi_j - \Phi)^2} = \frac{1}{(\dot{\gamma} - \dot{\gamma}_\infty)^2} \quad \text{with} \quad \dot{\gamma}_\infty = \frac{1}{C_B \cdot t_d} \left(\frac{\Phi_0 - \Phi}{\Phi - \Phi_m} \right) \quad (20)$$

547 The asymptotic value of the shear rate $\dot{\gamma}_\infty$ is given by Eq.(20). The dotted curve of Fig.12(a) for
 548 $\Phi=0.64$ is obtained with $C_B \cdot t_d=0.3s$, giving $\dot{\gamma}_\infty = 2.73 s^{-1}$ and the one of Fig.12(b) for $\Phi=0.66$
 549 with $C_B \cdot t_d=0.7s$. giving $\dot{\gamma}_\infty = 0.43 s^{-1}$. Note that it is the product $C_B \cdot t_d$ which can be obtained
 550 from the fit of the experimental curve and not each parameter separately. With this modification
 551 of the W-C model we have now a good agreement with the experiment. Still we are using the
 552 equilibrium value $f_{eq}(\sigma_r)$ and not its time evolution described by Eq.(18). It is only by
 553 considering this time evolution together with the introduction of the inertia of the rotating part
 554 that we can describe the fluctuations of the shear rate above the DST transition and obtain
 555 separately the parameters t_d and C_B . This is beyond the scope of this paper but we have verified
 556 that with the use of Eq. (18) the oscillating regime continue above the jamming volume fraction
 557 predicted by the W-C model (cf. Appendix B). On the other hand, we do not have an oscillating
 558 regime at $\Phi=0.58$ and below because despite a negative differential viscosity, its absolute value
 559 is not large enough to reach the theoretical criteria of instability that can be obtained by a linear
 560 stability analysis⁶³.

561 The qualitative explanation of the absence of jamming and of the persistence of the oscillations
 562 of the shear rate at high stresses is stated in the following. When the stress is high enough to set
 563 the particles in solid contact despite the presence of a stabilizing repulsive layer, a solid network
 564 of particles is formed which impedes the flow by connecting the walls of the cell. Nevertheless,
 565 in the absence of flow the applied stress which is now a contact stress (in comparison to a
 566 hydrodynamic one) will not be able to keep unchanged this static solid network, because the
 567 shear flow was responsible for the expulsion of the stabilizing polymer layer. In the absence of
 568 shear, the thermodynamic forces related to the energy of adsorption of the polymer molecules,

569 will no longer be opposed by the drag forces coming from the shear flow, so the polymer can
570 come back on the surfaces in the contact area and generate a pressure which will separate the
571 surfaces in the contact zone. It is also likely that, in hydrophilic suspensions with charged
572 surfaces, a layer of water molecules remains attached on the surface, even inside the frictional
573 contacts, and contributes to facilitate the breakdown of the frictional network in the absence of
574 a shear flow. The same process can also be present and even stronger, when the stabilizing force
575 is due to an ionic double layer since in the absence of shear flow, the counterions will be
576 attracted back to the surfaces and separate them. Once the network of frictional contacts is
577 broken, the shear flow begins to grow until the shear forces dominate the repulsive ones
578 initiating the jamming of the suspension and the cycle begins again. As briefly described in
579 annex B, the typical period of the oscillations is $T=0.1s$, so the amplitude of the oscillations
580 observed experimentally depends on the time of acquisition of the shear rate and is in reality
581 much higher than reported here at an acquisition rate of 1 point/s
582

583 In practice, above a few kPa, due to the centrifugal force and also to the presence of a normal
584 force σ_{rr} , transmitted through the percolated network, the interface with air becomes irregular
585 with extrusion of “granules“ and intrusion of air bubbles. This mechanism exists as well in
586 plate-plate geometry and in cylindrical Couette geometry ²⁵ and prevents to get reliable results
587 at very high stresses even in cylindrical Couette geometry.

588 Before passing to the effect of the magnetic field, from these comparisons between
589 experiments at three typical volume fractions we can already retain the following conclusions:
590 1) From the measurement of the electric resistance of the suspension it is possible to follow the
591 formation of the network of frictional contacts when increasing the stress.

592 2)-It is not possible to represent the rheological curve at every volume fraction with the same
593 values of the function $f(\sigma_r)$: if the parameter $q=1.16$ (obtained in some numerical simulations)
594 of the stretched exponential can describe the curve at $\Phi=0.58$, this is clearly not the case at
595 $\Phi=0.64$ and at $\Phi=0.66$ there is no shear thickening at all before the transition, leading to a
596 Heaviside function. It is the expression of the fact that we pass abruptly from a Bingham or
597 even a shear thinning behaviour ($p<1$) to the DST transition.

598 3) The non-zero average shear rate at high stress is explained by the fact that the frictional
599 contacts are unstable at zero shear rate.

600
601
602
603

604 **IV. EFFECT OF THE MAGNETIC FIELD ON THE DST** 605 **TRANSITION**

606 We have shown in preceding papers ^{37,67} that the application of a magnetic field on a suspension
607 of carbonyl iron particles at high volume fraction could considerably shift the critical shear rate
608 of the DST transition towards lower values. We also remarked that the difference between the
609 critical stress and the yield stress remained approximately constant in the range of field we have
610 used ⁶⁴. We shall try in this section to understand the physical process which could explain this
611 behaviour. In the following figures, Figs.14(a) and 14(b), we have plotted the raw curves
612 obtained in plate-plate geometry and below the differential viscosity $\frac{\partial \sigma}{\partial \dot{\gamma}}$ determined from the
613 corrected curve as defined by Eq.(4)

614

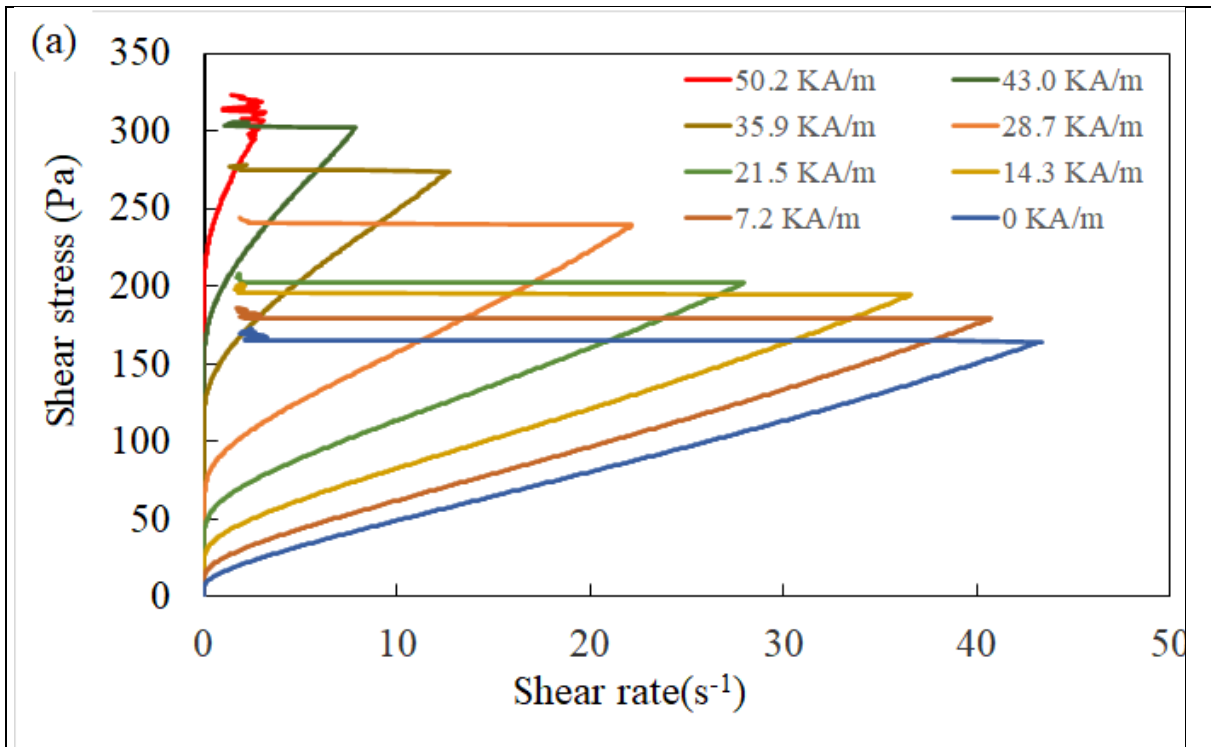


Fig. 14(a) $\Phi=0.63$. Evolution of the DST with the magnetic field. Raw curves; plate-plate geometry

615

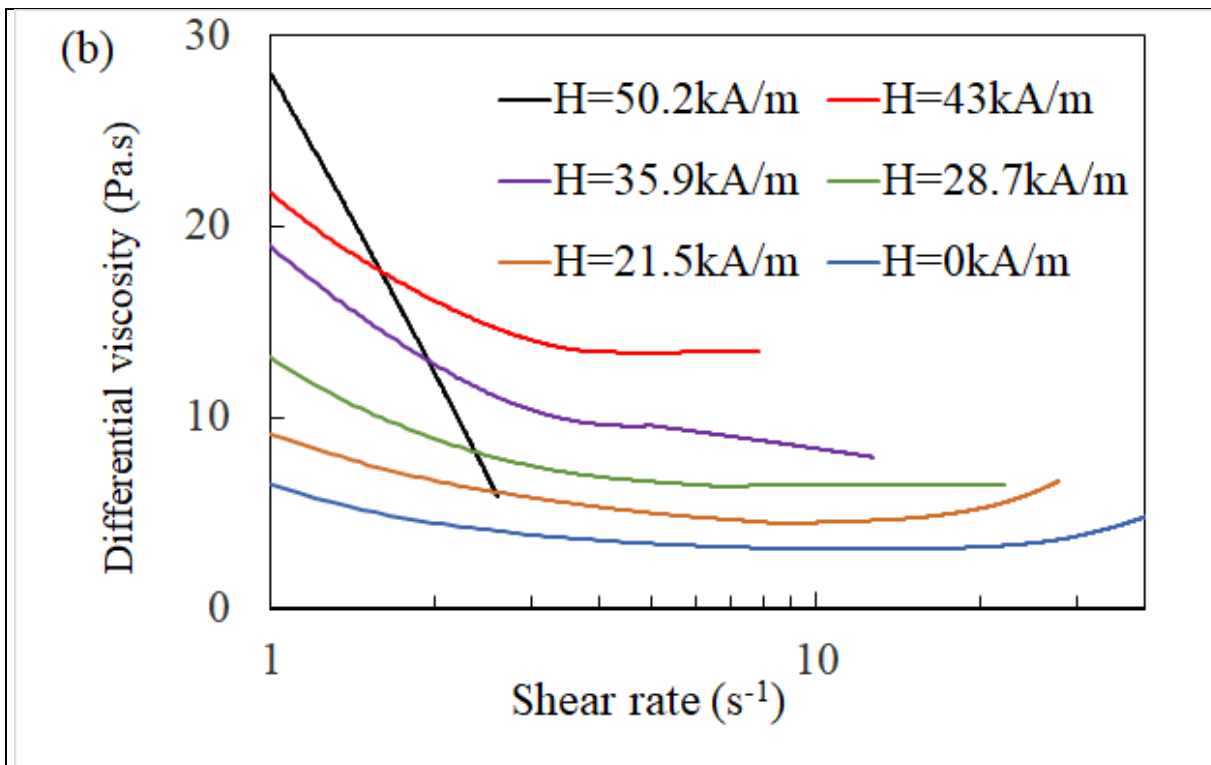


Fig. 14(b) $\Phi=0.63$. Differential viscosity for some of the rheograms represented in Fig.14(a)

616

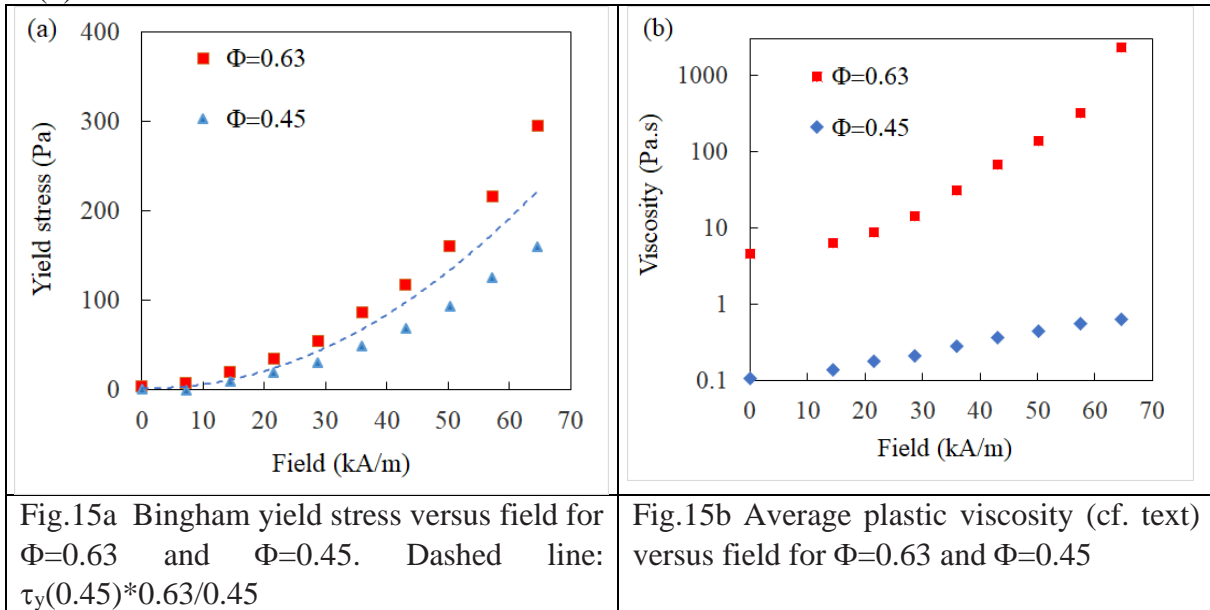
617

618

619

The more remarkable result is that, increasing the magnetic field, we pass from a behaviour which is first shear thinning and then shear thickening to a behaviour where we have only shear thinning before the DST transition (cf. Fig. 14(b)). This is like what we observe in the absence

620 of the field when we increase the volume fraction. Once again, in the frame of the W-C model,
 621 this is only possible if the function $f(\sigma_r)$ rises suddenly from zero to one at the transition (cf.
 622 Fig. 13). The shear thickening part which precedes the DST transition at low field or low
 623 volume fraction is more usual and can be interpreted as the formation of small clusters due to
 624 frictional contacts provoked at high shear by the removal of the layer of polymer from the
 625 surface⁵⁶. Some more information on the role of the polymer layer can be inferred from the
 626 comparison of the evolution of the yield stress and of the plastic viscosity with the magnetic
 627 field at intermediate and high-volume fraction. This is shown respectively in Figs 15(a) and
 628 15(b).



629 For the yield stress, the difference between the two volume fractions is not important. If we
 630 consider the simplified model of independent chains of particles spanning the gap between the
 631 two plates, the yield stress should be just proportional to the number of chains, that is to say, to
 632 the volume fraction; the dashed line is the extrapolation for $\Phi=0.63$ from $\Phi=0.45$ if it was the
 633 case. Even if the experimental values grow slightly faster (red squares), the difference is not so
 634 big and easy to explain because the model of individual chains is no longer valid at high volume
 635 fractions since the number of contacts per particles- and so the magnetic attractive force
 636 between pairs of particles- is expected to increase with the volume fraction. On the contrary the
 637 increase of viscosity with the intensity of the magnetic field is about 3 orders of magnitude at
 638 $\Phi=0.63$ against one order of magnitude at $\Phi=0.45$. The viscosity in Fig.15(b) is an average
 639 plastic viscosity: $\eta_{63} = (\sigma_c - \tau_y)/\dot{\gamma}_c$ for $\Phi=0.63$ and $\eta_{45} = (\sigma(400s^{-1}) - \tau_y)/400$ for
 640 $\Phi=0.45$. We must emphasize that the range of applied stress is about the same at $\Phi=0.63$ as at
 641 $\Phi=0.45$ but it is the range of shear rate which is much larger at $\Phi=0.45$ than at $\Phi=0.63$. This
 642 unexpected large increase of the viscosity with the field is an important observation for two
 643 reasons. First, it will allow to trigger the viscosity of this magnetorheological fluid with a much
 644 larger efficiency than with usual ones based on suspensions of intermediate volume fractions
 645 and second it helps to understand the process leading to DST in the presence of polymer
 646 brushes. The interaction between two layers of polymer brushes has been extensively studied
 647^{68,69} mainly because of their applications to reduce the viscosity of concentrated suspensions of
 648 mineral particles as, for instance, in cement industry. The repulsive force of entropic origin
 649 between the tails of the polymers prevents the particles from aggregation in the presence of
 650 attractive Van Der Waals forces. This osmotic force depends on many factors like the size
 651 distribution and the conformation of the polymer its energy and density of adsorption; its
 652

653 miscibility with the suspending fluid (the Flory parameter). A key parameter which derives
654 from these characteristics is the interpenetration zone of width, δ , of the layers of polymer and
655 its dependence on the applied hydrodynamic (and magnetic in our case) stress . If δ remains
656 small, then the system is equivalent to a hard sphere suspension with a renormalized volume
657 fraction, Φ_{eff} -incorporating the thickness of the polymer layer and a short-range repulsive force.
658 If the interparticle force, generated by the externally imposed stress, increases, the value of δ
659 will also increase in an extent depending of the stiffness of the repulsive force and also of a
660 Weissenberg number $W = \tau \cdot \dot{\gamma}$ where τ is the relaxation time of an adsorbed polymer. If $W < 1$
661 the polymer has the time to recover its equilibrium shape between the next collision with
662 another polymer; then the shear force generated by the collisions between monomers in the
663 interpenetration zone grows proportionally to the shear rate⁷⁰. It means that in this regime we
664 can have a Newtonian behaviour but with a viscosity which will depend on the field since
665 increasing the field will increase the interpenetration zone. On the contrary if $W > 1$ the polymers
666 do not have time to relax: they remain stretched by the shear flow which will decrease the
667 interpenetration zone and give a shear thinning behaviour or even an absence of dependence of
668 the shear if the interpenetration zone remains very weak. The relaxation time of the polymer
669 can be estimated from the Rouse model for PEO polymer in water⁷¹: $\tau = 0.0142N^2\xi b^2/kT$.
670 With $N=44$ the number of units of PEO, ξ the friction coefficient on one unit and $b=0.526\text{nm}$
671 the length of one unit. Considering that the viscosity of our suspending fluid is 10 times the one
672 of water we get $\tau \sim 10^{-6}\text{s}$. Another estimation based on Zimm theory⁷² gives $\tau = 5.11 R^3\eta_s/kT$
673 with R the root mean square separation of the extremities of a polymer and $\eta_s = 0.011\text{Pas}$,
674 the viscosity of the suspending fluid. Taking into account the expansion of the polymer due to
675 its compression by its neighbours we have $R=6\text{nm}$ ⁴² and in this case $\tau=2.6 \cdot 10^{-6}\text{s}$. This order of
676 magnitude means that, with this small polymer, we shall always have $W \ll 1$ and so that we
677 should remain in a Bingham regime with a plastic viscosity independent of the shear rate. This
678 is roughly what we observe above 3 s^{-1} except for the highest field where we have a continuous
679 shear thinning (cf. Fig.14(b)). This change of regime at high compression could be due to a
680 structural change of the compressed layer perhaps related to a beginning of desorption of the
681 polymer before the DST transition. On the other hand, the shear thinning observed at $\dot{\gamma} < 3\text{s}^{-1}$
682 is simply due to the progressive rupture of the aggregates formed by the attractive magnetic
683 forces.
684 If we call η_b the viscosity of these bilayers of polymers which separate the surfaces of the
685 particles it is likely that, at high volume fraction, where the polymer layers are always
686 interpenetrated, we could approximate the total viscosity as $\eta = \eta_{\text{HS}} \cdot \eta_b$ where η_{HS} is the relative
687 viscosity of the hard sphere suspension without coating polymers. Finally, increasing the field
688 increases a lot the plastic viscosity and to a much less extent the yield stress - which is the stress
689 necessary to separate the particles against the attractive magnetic force. On the other hand, the
690 stress needed to sweep the polymer layer out of the surface in the lubricated zone is essentially
691 the shearing stress coming from the relative motion of the particles

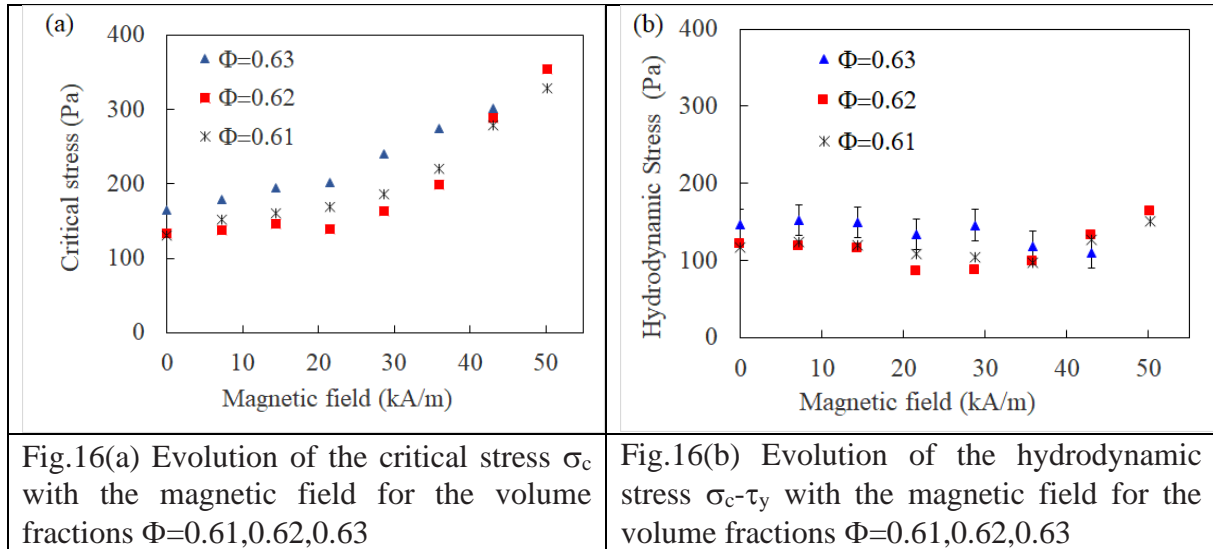


Fig.16(a) Evolution of the critical stress σ_c with the magnetic field for the volume fractions $\Phi=0.61,0.62,0.63$

Fig.16(b) Evolution of the hydrodynamic stress $\sigma_c - \tau_y$ with the magnetic field for the volume fractions $\Phi=0.61,0.62,0.63$

692 . This is the reason why it is the difference between the critical stress and the yield stress which
693 remains approximately constant when we increase the magnetic field instead of the critical
694 stress as we can see in Figs. 16(a) and 16(b).

695 The attractive force induced by the magnetic field contributes to increase the interpenetration
696 of the polymer. Consequently, the viscosity related to the shearing forces between the
697 interpenetrated parts of the polymer increases, until the shearing stress needed to wipe the
698 polymer out of the surface is reached. In this process the yield stress generated by the magnetic
699 force between the iron particles does not contribute directly to the shearing force acting on the
700 polymer layer which is alone responsible for the desorption of the polymer and the DST
701 transition.

702 V. CONCLUSION

703
704 Using a suspension of ferromagnetic particles stabilized by a superplasticizer molecule used in
705 cement industry, we have obtained a discontinuous shear thickening in a broad range of volume
706 fraction ($0.54 < \Phi < 0.67$). From the divergence of the low shear rate viscosity with the volume
707 fraction and from the use of the size distribution of the particles, we have deduced the two
708 volume fractions Φ_0 and Φ_j^t on which are based the Wyart-Cates model of DST. This model
709 also introduces the function $f(\sigma_r)$ representing the fraction of frictional contact versus the stress;
710 we have modelled this function with the help of two parameters λ and q ; this last one depicting
711 the sharpness of the transition. These two parameters are obtained from the constraint that the
712 experimental curve passes through the critical point where the shear rate begins to decrease.
713 Whereas simulations predict that this function remains independent of the volume fraction, we
714 find that it fits the one obtained in simulation, only in the domain of soft DST transition at the
715 lowest volume fractions where there is a second regime of constant viscosity. At highest volume
716 fraction the transition is sharper and finally becomes steplike. This last behaviour is related to
717 the fact that there is no shear thickening before the transition, which implies that $f(\sigma_r)=0$ for
718 $\sigma_r < 1$. The measurement of the electric resistance together with the stress/shear rate curve allows
719 to confirm the onset of a percolated network of frictional contacts associated to the decrease of
720 the shear rate and the fact that the expansion of this network with the stress depends strongly
721 on the volume fraction, contrary to the predictions of the numerical simulations. A numerical
722 model introducing a repulsive force depending on the interpenetration of the polymer together
723 with a criteria for the desorption of the polymer should allow to recover this behaviour.

724
725 Contrary to the W-C model which predicts the existence of a domain of jamming above
726 the DST transition, we do not observe it experimentally but rather the shear rate remains, on

727 average, constant above the critical stress. We were able to reproduce this behaviour by
 728 introducing a relaxation time, t_d , of the frictional contacts at zero shear rate expressed in Eq.(18).
 729 The resulting asymptotic shear rate $\dot{\gamma}_\infty$ (Eq.(20)) gives access to the product $C_B t_d$ where C_B is a
 730 constant associated to the collision rate between particles. The independent determination of
 731 these two parameters could be done through the analysis of the period of oscillations of the
 732 shear rate above the transition.

733 We have explained qualitatively the evolution of the rheology in the presence of the
 734 magnetic field by its effect on the interpenetration of the polymer layer adsorbed on the surface
 735 of the particles, in particular the strong increase of plastic viscosity for small amplitudes of
 736 magnetic field. The evolution of the polymer layers with their progressive interpenetration and
 737 their desorption above a given shearing stress makes the particle short range interactions much
 738 more complicated than the "critical load model" CLM model used in computer simulations, so
 739 it is not surprising that some predictions of these numerical models do not apply to our
 740 experimental systems. In order to get more information on the interparticle forces in the
 741 presence of brush polymer it would be useful to make experiments on a pair of iron
 742 microparticles with the help of a force apparatus⁵⁷. At last, we want to emphasize that this
 743 magnetorheological fluid, based on very high-volume fraction of iron particles thanks to this
 744 superplasticizer, is much more efficient than usual ones because of two physical phenomena:
 745 the DST transition and the increase of viscosity due to the interpenetration of the polymer
 746 brushes. The increase of yield stress with the field which is the usual mechanism in conventional
 747 MR fluid is of course present but not more than in usual MR fluids.

748
749

750 APPENDIX A: Theoretical packing of a polydisperse suspension

751

752 For a suspension of monosized frictionless hard spheres the maximum flowing volume fraction
 753 is the well-known random close packing $\Phi_{RCP}=0.637$. For a polydisperse suspension, we use
 754 an expression based on the three first moments of the distribution⁴⁰:

$$755 \frac{\Phi_0}{1-\Phi_0} = \frac{M_3}{M_1 M_2^2} \frac{\Phi_{RCP}}{1-\Phi_{RCP}} \quad \text{where } M_k = \int_0^\infty a^k P(a) da \quad (A-1)$$

756

757 By taking the moments M_k from the experimental size distribution, one gets $\frac{M_3}{M_1 M_2^2} = 1.19$ and
 758 from Eq. (A-1), we find $\Phi_0=0.676$ for the maximum flowing fraction. Another way to obtain
 759 Φ_0 is to relate the lognormal distribution to a bidisperse suspension characterized by the two
 760 sizes of the particles and their relative amounts. This relation implies to preserve the same mean
 761 radius, the same polydispersity and skewness for the lognormal and the bidisperse distribution
 762⁴¹. In our case, we find respectively for the small and large particles $a_s=0.223\mu m$, $a_L=0.715\mu m$
 763 and a ratio of large particles: $X_L=0.149$. An analytical expression for the random close packing
 764 of a bidisperse suspension was given by H.J.H. Brouwers⁴² (cf their Eq.(16) with $\beta^{rcp}=0.2$ and
 765 $\beta^{rp}=0.16$). Using their expression for small values of $u=a_s/a_L$ corresponding to our situation, we
 766 obtain $\Phi_0=0.683$.

767 For the estimation of Φ_j'' , we start from the theoretical values $\Phi_j'' \sim 0.55-0.56$ for monodisperse
 768 suspensions and we use them instead of Φ_{RCP} in Eq.(A-1) for the transposition to our
 769 polydisperse suspension, giving $\Phi_j'' \sim 0.592 - 0.602$. Using the second model based on the
 770 analogy with the bidisperse model, we find $\Phi_j'' \sim 0.581 - 0.592$.

771

772

773 **APPENDIX B: Shear rate fluctuations behind DST**

774 The equation of motion of the rotating tool of the rheometer is the following:

775
$$I \frac{d^2\theta}{dt^2} + T_v = T_a \quad \text{with} \quad T_v = \frac{\pi R^3}{2} \sigma + \frac{2\pi R^3}{3} \tau_y \quad \text{and} \quad T_a = \frac{\pi R^3}{2} \sigma_a \quad (\text{B-1})$$

776

777 I represent the inertia moment of the rotating part (motor +tool).

778 T_v is the viscous torque of a Bingham fluid on the disk of radius R.

779 T_a is the torque applied by the motor and σ_a , the stress given by the software of the
780 rheometer.

781 It is important to note that, due to inertia, the stress applied by the rheometer, σ_a , is
782 different from the one, σ , really applied to the suspension: $\eta\dot{\gamma} + \tau_y$ present in the function

783 $f_{eq}(\sigma/\sigma_c)$

784 Using the relation between the rim shear rate and the angular frequency: $\dot{\gamma} = \frac{d\theta}{dt} \frac{R}{h}$, Eq. B-

785 1 can be written as:

786
$$\ddot{\gamma} = \frac{2h}{\pi R^4 I} \left[\eta_{pl}(f) \dot{\gamma} + \frac{4}{3} \tau_y - \sigma_a \right] \quad (\text{B-2})$$

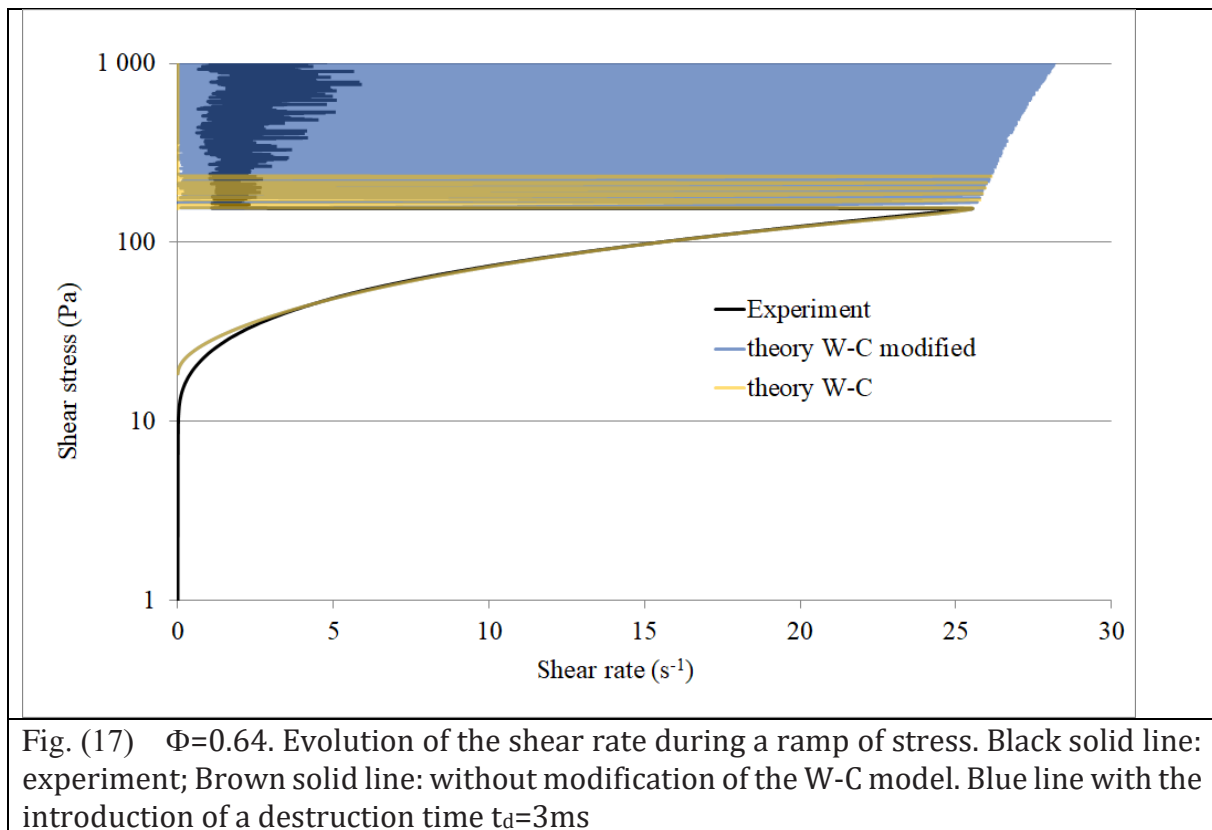
787 The evolution of the structural parameter, $f(t)$ was given by Eqs.(18)-(19):

788
$$\frac{\partial f}{\partial t} = -C_B \dot{\gamma} (f(t) - f(\sigma_r)) - \frac{f(t)}{t_d} \quad (\text{B-3})$$

789 And the viscosity dependence on f by Eq.(14):

790
$$\eta_{pl}(f) = \alpha_0 \left(1 - \frac{\Phi_{eff}}{\Phi_j(f)} \right)^{-2} \quad (\text{B-4})$$

791 We have reported in Fig. (17) the solution of the two coupled equations (B-2) and (B-3)
792 for $\Phi=0.64$ for two cases: one, where the destruction time is very large (in practice we
793 suppress the last term of Eq.(B-3)) and the second where $t_d=3\text{ms}$. Since, in the W-C model
794 the suspension is jammed above $\sigma=216\text{Pa}$, in the first case, the oscillations of the shear
795 rate stop at this level (yellow curve). On the contrary, in the presence of the destruction
796 time, t_d , the oscillations continue as we observe experimentally (blue curve). The fact that
797 the amplitude of the shear rate oscillations is much lower in the experiment compared to
798 the theory is due to the acquisition rate of the rheometer during the ramp of stress, which
799 is much smaller than the period of the oscillation (typically 0.1s). A faster sampling would
800 show the same amplitude of oscillation as the theoretical ones⁶³



801

802 ACKNOWLEDGMENTS

803 The authors want to thank the CENTRE NATIONAL D'ETUDES SPATIALES (CNES, the
 804 French Space Agency) for having supported this research. We want also to thank the center of
 805 electronic microscopy (CCMA) and F.Orange for the numerous and helpful SEM images of
 806 our particles.

807 REFERENCES

- 808 ¹ H.A. Barnes, *Journal of Rheology* **33**, 329 (1989).
 809 ² D. Quemada, *The European Physical Journal-Applied Physics* **2**, 175 (1998).
 810 ³ H. Freundlich and H.L. Röder, *Transactions of the Faraday Society* **34**, 308 (1938).
 811 ⁴ R.L. Hoffman, *Transactions of the Society of Rheology* **16**, 155 (1972).
 812 ⁵ M.K. Chow and C.F. Zukoski, *Journal of Rheology* **39**, 33 (1995).
 813 ⁶ H.M. Laun, R. Bung, and F. Schmidt, *Journal of Rheology* **35**, 999 (1991).
 814 ⁷ H.M. Laun, R. Bung, S. Hess, W. Loose, O. Hess, K. Hahn, E. Hädicke, R. Hingmann, F.
 815 Schmidt, and P. Lindner, *Journal of Rheology* **36**, 743 (1992).
 816 ⁸ J. Bender and N.J. Wagner, *Journal of Rheology* **40**, 899 (1996).
 817 ⁹ P. d'Haene, J. Mewis, and G.G. Fuller, *Journal of Colloid and Interface Science* **156**, 350
 818 (1993).
 819 ¹⁰ A. Fall, N. Huang, F. Bertrand, G. Ovarlez, and D. Bonn, *Phys. Rev. Lett.* **100**, 018301
 820 (2008).
 821 ¹¹ R.G. Egres and N.J. Wagner, *Journal of Rheology* **49**, 719 (2005).
 822 ¹² M. Neuville, G. Bossis, J. Persello, O. Volkova, P. Boustingorry, and M. Mosquet, *Journal*
 823 *of Rheology* **56**, 435 (2012).
 824 ¹³ C.E. Chaffey and I. Wagstaff, *Journal of Colloid and Interface Science* **59**, 63 (1977).

825 ¹⁴ W.J. Frith, P. d’Haene, R. Buscall, and J. Mewis, *Journal of Rheology* **40**, 531 (1996).
826 ¹⁵ M.E. Fagan and C.F. Zukoski, *Journal of Rheology* **41**, 373 (1997).
827 ¹⁶ D. Lootens, H. Van Damme, and P. Hébraud, *Phys. Rev. Lett.* **90**, 178301 (2003).
828 ¹⁷ V.T. O’Brie and M.E. Mackay, *Langmuir* **16**, 7931 (2000).
829 ¹⁸ W.H. Boersma, P.J.M. Baets, J. Laven, and H.N. Stein, *Journal of Rheology* **35**, 1093
830 (1991).
831 ¹⁹ G.V. Franks, Z. Zhou, N.J. Duin, and D.V. Boger, *Journal of Rheology* **44**, 759 (2000).
832 ²⁰ R.J. Larsen, J.-W. Kim, C.F. Zukoski, and D.A. Weitz, *Physical Review E* **81**, 011502
833 (2010).
834 ²¹ H.M. Laun, *Journal of Non-Newtonian Fluid Mechanics* **54**, 87 (1994).
835 ²² D. Lootens, H. van Damme, Y. Hémar, and P. Hébraud, *Phys. Rev. Lett.* **95**, 268302
836 (2005).
837 ²³ E. Brown and H.M. Jaeger, *Journal of Rheology* **56**, 875 (2012).
838 ²⁴ N.Y. Lin, B.M. Guy, M. Hermes, C. Ness, J. Sun, W.C. Poon, and I. Cohen, *Physical Review*
839 *Letters* **115**, 228304 (2015).
840 ²⁵ M.E. Cates, M.D. Haw, and C.B. Holmes, *Journal of Physics: Condensed Matter* **17**,
841 S2517 (2005).
842 ²⁶ R. Seto, R. Mari, J.F. Morris, and M.M. Denn, *Physical Review Letters* **111**, 218301
843 (2013).
844 ²⁷ R. Mari, R. Seto, J.F. Morris, and M.M. Denn, *Journal of Rheology* **58**, 1693 (2014).
845 ²⁸ A. Singh, R. Mari, M.M. Denn, and J.F. Morris, *Journal of Rheology* **62**, 457 (2018).
846 ²⁹ B.J. Maranzano and N.J. Wagner, *Journal of Rheology* **45**, 1205 (2001).
847 ³⁰ A. Fall, A. Lemaitre, F. Bertrand, D. Bonn, and G. Ovarlez, *Physical Review Letters* **105**,
848 268303 (2010).
849 ³¹ E. Brown and H.M. Jaeger, *Reports on Progress in Physics* **77**, 046602 (2014).
850 ³² M. Wyart and M.E. Cates, *Physical Review Letters* **112**, 098302 (2014).
851 ³³ Y.-F. Lee, Y. Luo, S.C. Brown, and N.J. Wagner, *Journal of Rheology* **64**, 267 (2020).
852 ³⁴ M. Wang, S. Jamali, and J.F. Brady, *Journal of Rheology* **64**, 379 (2020).
853 ³⁵ R. Tadmor, J. Janik, J. Klein, and L.J. Fetters, *Physical Review Letters* **91**, 115503
854 (2003).
855 ³⁶ A.V.N. Le, A. Izzet, G. Ovarlez, and A. Colin, (2022).
856 ³⁷ G. Bossis, Y. Grasselli, A. Meunier, and O. Volkova, *Applied Physics Letters* **109**,
857 111902 (2016).
858 ³⁸ N.Y. Lin, C. Ness, M.E. Cates, J. Sun, and I. Cohen, *Proceedings of the National Academy*
859 *of Sciences* **113**, 10774 (2016).
860 ³⁹ C.-P. Hsu, J. Mandal, S.N. Ramakrishna, N.D. Spencer, and L. Isa, *Nature*
861 *Communications* **12**, 1 (2021).
862 ⁴⁰ A. Santos, S.B. Yuste, M.L. de Haro, G. Odriozola, and V. Ogarko, *Physical Review E* **89**,
863 040302 (2014).
864 ⁴¹ S. Pednekar, J. Chun, and J.F. Morris, *Journal of Rheology* **62**, 513 (2018).
865 ⁴² H.J.H. Brouwers, *Physical Review E* **87**, 032202 (2013).
866 ⁴³ G. Bossis, P. Boustingorry, Y. Grasselli, A. Meunier, R. Morini, A. Zubarev, and O.
867 Volkova, *Rheologica Acta* **56**, 415 (2017).
868 ⁴⁴ M. Hermes, B.M. Guy, W.C. Poon, G. Poy, M.E. Cates, and M. Wyart, *Journal of Rheology*
869 **60**, 905 (2016).
870 ⁴⁵ R.J. Larsen, J.-W. Kim, C.F. Zukoski, and D.A. Weitz, *Rheologica Acta* **53**, 333 (2014).
871 ⁴⁶ A. Fall, F. Bertrand, D. Hautemayou, C. Mézière, P. Moucheront, A. Lemaitre, and G.
872 Ovarlez, *Physical Review Letters* **114**, 098301 (2015).
873 ⁴⁷ N. Kchit and G. Bossis, *Journal of Physics D: Applied Physics* **42**, 105505 (2009).

874 ⁴⁸ S. Fazekas, J. Török, and J. Kertész, *Physical Review E* **75**, 011302 (2007).
875 ⁴⁹ G. Ovarlez, F. Bertrand, and S. Rodts, *Journal of Rheology* **50**, 259 (2006).
876 ⁵⁰ F. Boyer, É. Guazzelli, and O. Pouliquen, *Phys. Rev. Lett.* **107**, 188301 (2011).
877 ⁵¹ C. Ness and J. Sun, *Soft Matter* **12**, 914 (2016).
878 ⁵² R. Radhakrishnan, J.R. Royer, W.C.K. Poon, and J. Sun, *Granular Matter* **22**, 29 (2020).
879 ⁵³ B.M. Guy, M. Hermes, and W.C. Poon, *Physical Review Letters* **115**, 088304 (2015).
880 ⁵⁴ J.R. Royer, D.L. Blair, and S.D. Hudson, *Physical Review Letters* **116**, 188301 (2016).
881 ⁵⁵ J. Klein, E. Kumacheva, D. Mahalu, D. Perahia, and L.J. Fetters, *Nature* **370**, 634 (1994).
882 ⁵⁶ U. Raviv, R. Tadmor, and J. Klein, *The Journal of Physical Chemistry B* **105**, 8125
883 (2001).
884 ⁵⁷ J. Comtet, G. Chatté, A. Niguès, L. Bocquet, A. Siria, and A. Colin, *Nature*
885 *Communications* **8**, 1 (2017).
886 ⁵⁸ M. Jerkins, M. Schröter, H.L. Swinney, T.J. Senden, M. Saadatfar, and T. Aste, *Phys. Rev.*
887 *Lett.* **101**, 018301 (2008).
888 ⁵⁹ L.E. Silbert, *Soft Matter* **6**, 2918 (2010).
889 ⁶⁰ A. Singh, S. Pednekar, J. Chun, M.M. Denn, and J.F. Morris, *Physical Review Letters* **122**,
890 098004 (2019).
891 ⁶¹ H.B. Cheng, L. Zuo, J.H. Song, Q.J. Zhang, and N.M. Wereley, *Journal of Applied Physics*
892 **107**, 09B507 (2010).
893 ⁶² Y.D. Liu and H.J. Choi, *Materials Research Bulletin* **69**, 92 (2015).
894 ⁶³ G. Bossis, O. Volkova, Y. Grasselli, and O. Gueye, *Philosophical Transactions of the*
895 *Royal Society A* **377**, 20180211 (2019).
896 ⁶⁴ J.A. Richards, J.R. Royer, B. Liebchen, B.M. Guy, and W.C.K. Poon, *Phys. Rev. Lett.* **123**,
897 038004 (2019).
898 ⁶⁵ A.S. Baumgarten and K. Kamrin, *Proceedings of the National Academy of Sciences* **116**,
899 20828 (2019).
900 ⁶⁶ G. Bossis, Y. Grasselli, and O. Volkova, *Rheol Acta* **61**, 1 (2022).
901 ⁶⁷ G. Bossis, Y. Grasselli, A. Meunier, and O. Volkova, *Journal of Intelligent Material*
902 *Systems and Structures* **1** (2017).
903 ⁶⁸ P.A. Schorr, T.C. Kwan, S.M. Kilbey, E.S. Shaqfeh, and M. Tirrell, *Macromolecules* **36**,
904 389 (2003).
905 ⁶⁹ S. de Beer, E. Kutnyanszky, M.H. Müser, and G.J. Vancso, *JoVE (Journal of Visualized*
906 *Experiments)* e52285 (2014).
907 ⁷⁰ T. Kreer, *Soft Matter* **12**, 3479 (2016).
908 ⁷¹ E. Rognin, N. Willis-Fox, T.A. Aljohani, and R. Daly, *Journal of Fluid Mechanics* **848**, 722
909 (2018).
910 ⁷² R.G. Larson, *The Structure and Rheology of Complex Fluids* (Oxford university press
911 New York, 1999).
912